Surface Tension Prevails Over Solute-Effect in Organic-Influenced

Cloud Droplet Activation

1   Environmental Information

1.1   Meteorology

For the events discussed in this paper, the air mass was classified *mP* (maritime polar) in origin as illustrated in Fig. S1.1.1 where four-day back trajectories are displayed. The trajectories at 100 m, 1000 m and 2000 m remain at a constant level for the four days suggesting entrainment and/or vertical exchange was at a minimum. Wind LIDAR data at Mace Head reveal minimal turbulence and low updraft velocities. Very low black carbon concentration (below 5 ng m^{-3}) indicates an extremely clean air mass arriving at Mace Head, thus pointing to negligible contribution from anthropogenic sources. Wind speed was ~ 5m s^{-1} and relative humidity at relatively low values of 70-80% for marine flow, which would be consistent with slightly-stable thermodynamic conditions associated with a high pressure (1020 hP) system to the southwest of Ireland (Fig. S1.1.2). HYSPLIT model did not indicate any precipitation along the trajectory. The events are typical of 'open ocean new particle production events' as classified by O'Dowd et al.[33], typically occurring in polar maritime air masses advecting over waters rich in blooming fields.
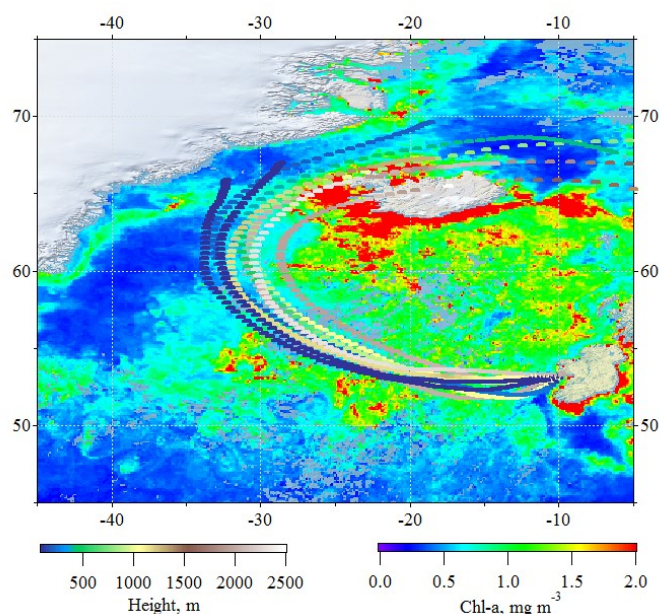

Figure S1.1.1 Air mass back-trajectories for the main event depicted in Fig. 2 overlaid on the chlorophyll-a map. Air mass back trajectories were calculated using Hybrid Single-Particle Lagrangian Integrated Trajectory, a transport and dispersion model developed by the NOAA Air Resources Laboratory[34]. Chl-a data were extracted from NASA Earth Observations dataset.
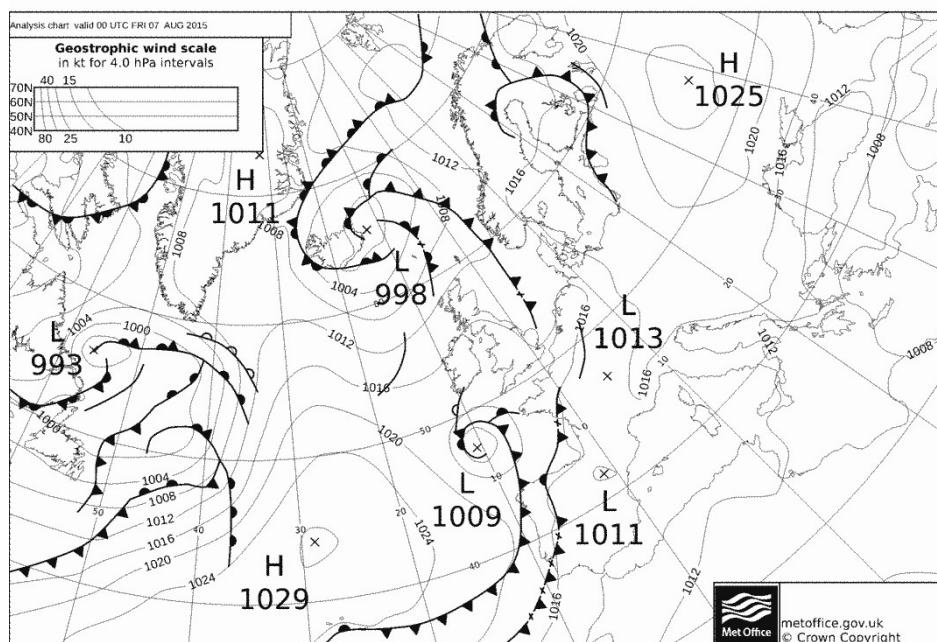
Figure S1.1.2. Meteorological map by UK Met Office for the 7th August 2015

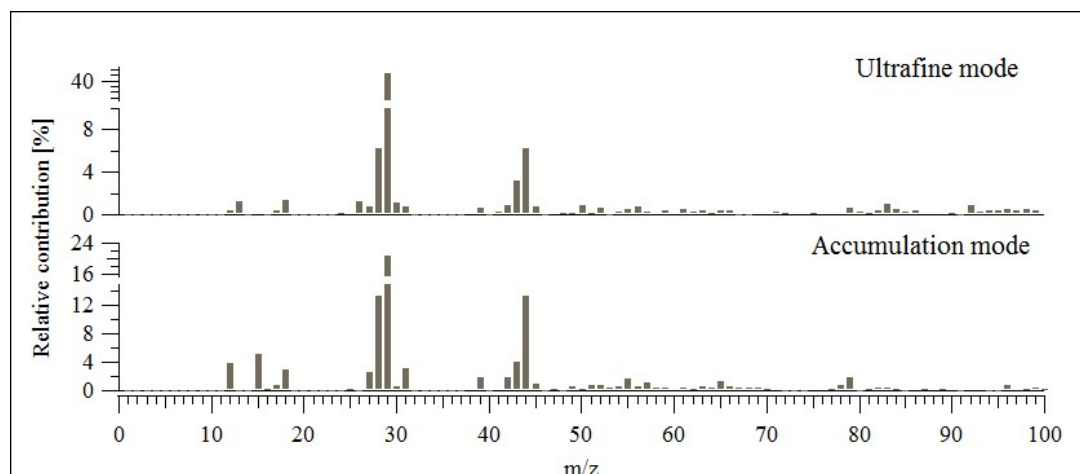## 1.2   AMS mass spectra for NUM event

Figure S1.2.1. Mass spectra of different aerosol modes: (top) ultrafine aerosol mode (NUM) (bottom) accumulation mode.

1.3   Weighted diameter (D_w)

The weighted diameter was obtained by summing up all SMPS size bins multiplied by their number concentration and dividing it by the total number concentration. For example, a

bimodal size distribution with a mode at 20 nm and 100 nm, both with equal number concentrations, would have a weighted average particle size of 60 nm. For almost unimodal distribution as was the case for the ultrafine event, the weighted diameter would represent the strongest ultrafine mode and would be ~30 nm.

2 Instrument Uncertainties & CCN Closure Sensitivity

2.1 Aerosol Mass Spectrometry Instrument Uncertainties

Aerosol chemical composition was measured using the Aerodyne Inc. High Resolution Time of Flight Aerosol Mass Spectrometer. The standard 1-minute resolution detection limits are reported by DeCarlo et al.[35] and are equal to 22, 5.2, 2.9, 38, and 12 ng m^{-3} for organic matter (OM), sulphate, nitrate, ammonium and chloride, respectively. For low concentrations the detection limit is analogous to the instrument's precision. This precision is insufficient to retrieve the NUM chemical composition; however, it can be improved by increasing the averaging time. Therefore, the AMS chemical mass size distributions were averaged over approximately 12 hours (i.e. the duration of the event), leading to a reduction (improvement) in the detection limit by more than a factor of 10 - calculations show a reduction in detection limit (DL) from 22 ng m^{-3} for OM at 1 min averaging time to 1 ng m^{-3} for averaging over a number of hours. Similar, but slightly larger, values were retrieved for this study from the size distributions of filter periods: 5 min DL were 73, 18, 10, 84 and 15 ng m^{-3} and 12 hour DL - 6, 1.5, 0.9, 7, and 1.2 for OM, sulphate, nitrate, ammonium and chloride, respectively.

Although the AMS precision is of the order of a few percent, the accuracy, mainly determined by the collection efficiency, is approximately 30-40%[36]. However, for determining the relative contributions of different chemical species, as we do in this manuscript, the instrument precision, or detection limit, matters more than the accuracy. The AMS accuracy is generally dominated by the collection efficiency; however, given that the NUM is internally-mixed (see below), the collection efficiency should be the same for both sulphate and organics, and thus, the accuracy should not impact on the determination of the relative ratio between the internally mixed sulphate and organics.

Uncertainties related to a relative ionization of organic matter are well summarised in a study by Jimenez et al.[37] The RIE (Relative Ionization Efficiency) of ambient organic mixtures, because of their complexity, would average out into standard OM RIE used in AMS data processing and equal to 1.4. Our study is indeed an ambient study that addresses aerosol formation and growth occurring hundreds of kilometres away from the sampling location and covering large ocean areas[38]. Therefore all averaging and complexity of OM described in

the Jimenez et al.[37] study applies here and 20% uncertainty of RIE[36] is applicable to the data presented in this manuscript. Moreover, this uncertainty limit or even a smaller one is confirmed by the data presented in the Figure S2.1.1. It shows a comparison of AMS-OM versus thermo-optical OC for both ambient marine (as in this study) and ambient anthropogenic organic aerosol. The RIE of 1.4 for the AMS-OM was applied and was valid for both marine aerosol (thus marine organics) and anthropogenic conditions. Data points (note that each single point comprises 1 week each of continuous sampling, e.g. two periods of clean marine air, and two periods of polluted air to different degrees) for marine organics lay on the same slope as long range processed organics transported to Mace Head.
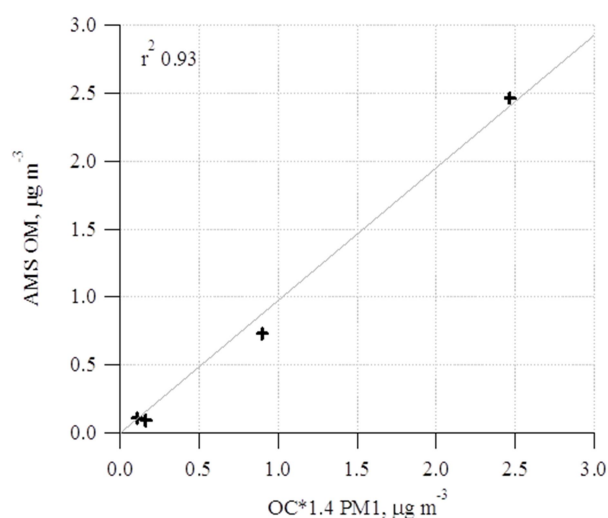

Figure S2.1.1. AMS-OM versus thermo-optical OC for both ambient marine (as in this study) and ambient anthropogenic organic aerosol where the RIE for the AMS-OM is 1.4.

Internal/external mixture. We assume the internal mixing based on analysis of 1 year's k-means cluster analysis of HTDMA data[39]. Our assumption on internal mixing is also based on observations of this particular NUM event where we compare the AMS vacuum aerodynamic diameter for both organic and sulphate mass distributions, and despite different densities associated with the individual compounds, the distributions exhibit a coincident mass modal diameter[40]. This can only be observed for an internal mixture while maintaining consistence with the observed SMPS volume mode. We further add, if the organo-sulphate NUM was externally mixed and produced from secondary particle formation (i.e. via nucleation and growth), separate sulphuric acid particles and organic particles would have to form probably simultaneously and grow at the same rate to produce two distinct NUMs with the same modal diameter but different chemical composition – this would require that organic vapours were only condensing on organic clusters and nano-particles, and similarly, sulphuric acid only condensing on sulphate particles. Alternatively, the particles are primary, but there is no production mechanism for primary sulphate nanoparticles over the ocean. The remaining option is that the sulphate mode is formed from secondary processes, and the organic is primary, and the sulphate vapours only condense on sulphate particles, which contradicts the physics of new particle formation and

growth as existing aerosol particles would act as a sink for the vapours and for nucleated clusters, thus inhibiting the nucleation of new atmospheric particles[41]. The only acceptable scenario is internal mixing – anything else is non-physical.

Despite the proportion of OM to SO_4 being insensitive to collection efficiency (CE), the CE would matter for the absolute values of chemical compounds, therefore, a composition-dependent CE^{42} was applied to the measurement periods discussed in this study, and consequently, the CE in this study ranged from 0.45 to 1 for different time periods and depended on nitrate availability and/or particle acidity. Relative humidity in the sample line was maintained at < 40 %, thus, did not have an additional effect on CE. In supporting tests, good agreement was found between the AMS total mass concentration and SMPS volume (Fig. S2.1.2) with a correlation coefficient R^2 being equal to 0.9. The small scatter between the AMS and SMPS data suggests an appropriate CE and chemical speciation correction (CE is dependent on the chemical composition); however, the deviation in the slope from the 1:1 line, which translates into density, points to either a small underestimation by AMS or small overestimation by SMPS.
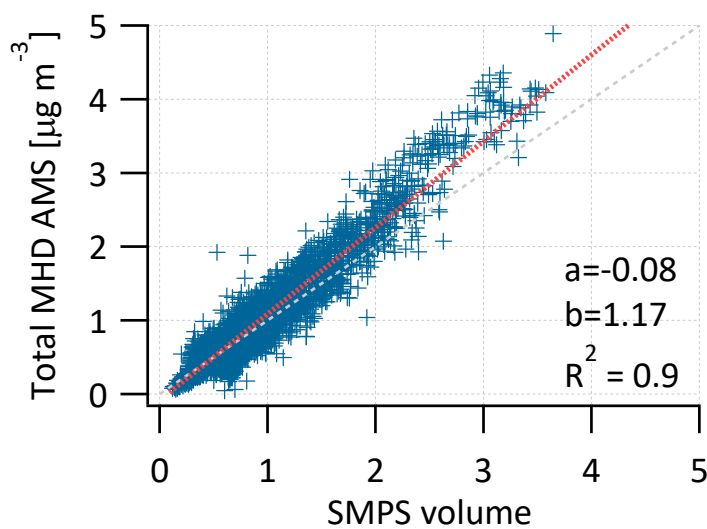

Figure S2.1.2 AMS total mass concentration vs. integrated SMPS volume.

Despite high mass resolution data used in this manuscript, size distributions were provided for unit mass resolution data as HR sizing is not easily achievable yet. This resulted in a poor quantification of ammonium size distribution as it has interferences with both water signal and gaseous phase, especially at the smaller sizes. Water significantly contributes to m/z's 16 and 17, and so does ammonium. Fragmentation tables were derived to address this issue for unit mass resolution; however, they cannot resolve the problem completely. This brings an ambiguity whether sulphate was ammonium sulphate or sulphuric acid in the NUM particles, therefore, chemical sensitivity analysis and modelling, presented in sections 2.3 and 3.7.2, addresses both sulphuric acid and ammonium sulphate composition.

Effective densities for NUM and ACCU modes were calculated by matching vacuum aerodynamic diameter (from AMS) to mobility diameter (from SMPS); the procedure is described in DeCarlo et al.[43]. These diameters are related by particle density, and assumptions on particle shape and internal mixture have to be made. This procedure resulted in NUM particle density equal to ~1.6 g cm^{-3} and ACCU to ~1.34 g cm^{-3}. Calculated SMPS mass, with densities derived from the diameter matching procedure, compared well with the AMS derived mass for both NUM and ACCU modes. However, densities for these modes can also be derived from chemical composition measured by AMS with known densities for sulphuric acid/ ammonium sulphate as well as organic matter. Considering volume proportions from AMS chemical composition, resulted in the following densities: 1.2 - 1.3 g cm^{-3} for NUM and 1.4 -1.5 g cm^{-3} for ACCU. There are several explanations for differences in densities calculated by different methods: higher density derived from diameter metrics than the one derived from the chemical composition, in NUM mode, can be explained by a presence of iodine/iodine oxides in the ultrafine mode, which possess density of 4.93 g cm^{-3} and were not quantified at this time; or uncertainty in AMS sizing; or deviation from spherical particle shape. Nonetheless, the difference between diameter derived density and chemical composition density is ~20 % and 11 % for NUM and ACCU accordingly, which is acceptable within instrument uncertainties.

2.2   Aerosol Sizing and Counting Instrument Uncertainties

Aerosol size distributions and integrated number concentrations were measured using a scanning mobility particle sizer (SMPS) system[44]. The system comprised of a differential mobility analyser (DMA, TSI model 3071), a condensation particle counter (TSI model 3010), and an aerosol neutralizer (TSI 3077) was scanned every 10 minutes. The MHD SMPS system follows the EUSAAR protocol for particle physical properties measurement (http://www.eusaar.net/files/activities/na3.cfm). EUSAAR protocols centre on the harmonisation of measurement procedures and data inversion routines for mobility size spectrometers (DMPS/SMPS) in order to ensure the most accurate retrievals of aerosol number size distributions in the range 10-500 nm diameter across all EUSAAR stations. The MHD SMPS is regularly calibrated according to these guidelines. Guidelines relate sample and sheath flow RH, pressure, T, stability, charging efficiency and diffusional losses. Prior to sampling to the SMPS, the aerosol flow for Mace Head instrument was dried to below 20 % relative humidity. The SMPS was also regularly calibrated using the standard TSI aerosol generation system. Immediately prior to the campaign, we compared a TSI aerosol generation/calibration system reconfigured into SMPS mode to run an intercomparison experiment between the MHD-EUSAAR protocol SMPS with the standard TSI configured SMPS (noting that the DMA columns are more or less the same).

The result of the intercomparison is shown in Fig. S2.2.1. The red curve is the MHD SMPS while the black is the TSI SMPS. While there are differences across the size distribution, the overall agreement is very good, being between 3% and 7% for the evaluated parameters (mode peak diameter and mode peak height). The higher concentrations seen in the MHD spectrum for the smallest and largest sizes relate to consideration of various sampling loss mechanisms occurring at these size ranges taken into account in the MHD-EUSAAR SMPS. The integrated total particle concentration measured by the two SMPS systems agreed with 10% of each other.
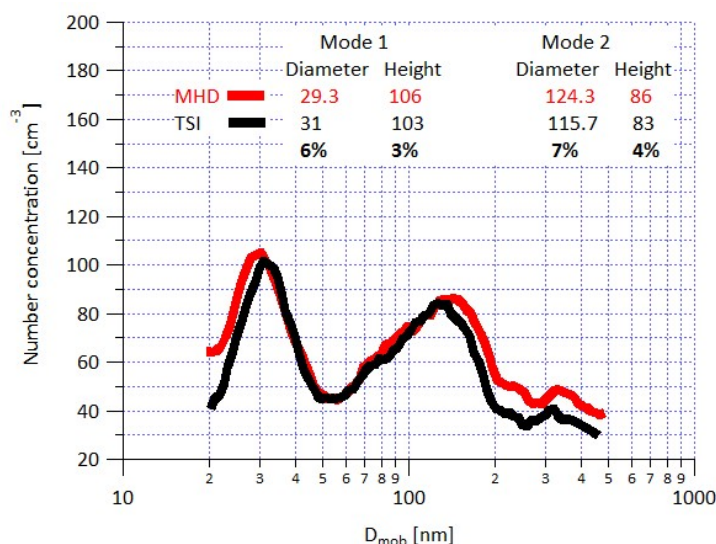

Figure S2.2.1. Comparison of Mace Head (MHD) and TSI 3080 (TSI) SMPS systems.

Given the nature of the SMPS instrument and its data inversion, small errors in sizing can amplify into large errors in total concentration; consequently, it is essential to have good agreement between parallel integrated total number concentration measurements. In other words, it is very unlikely to get agreement in total concentration if the SMPS is not operating in an optimal manner.

Accordingly, the MHD SMPS total number concentration was compared with a CPC (TSI model 3010) total concentration, which was sampling from the same community inlet. Fig. S2.2.2 indicates that two independent number concentration measurements agreed very well - on average, ~3% difference between SMPS and CPC number concentration, with the higher concentration coming from the SMPS. The difference is not systematic and more variability is seen in the SMPS total concentration (e.g. see Standard Deviation in figure box).
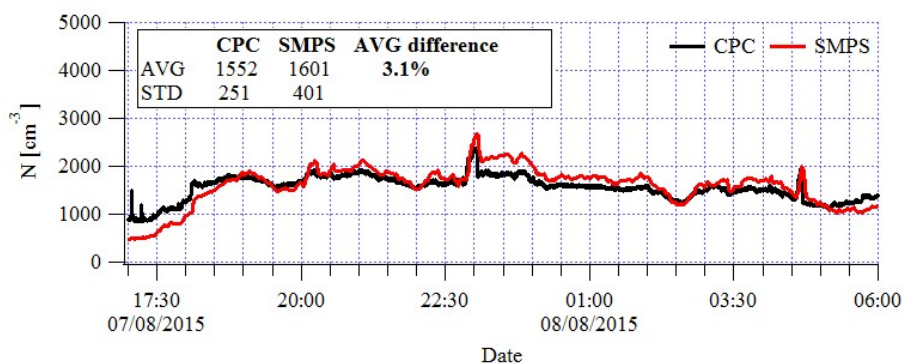
Figure S2.2.2. SMPS and CPC number concentrations during NUM event.

The intercomparison confirmed that MHD SMPS system errors were well within general uncertainties derived for this type of instrument (±10 % for size in the range of 20 -200 nm and ±4 % for number)[45].

2.3   CCN Closure and Sensitivity Analysis

An evaluation of closure sensitivity to instrument uncertainties was performed for the overall 4-week campaign, excluding NUM events, and separately for the NUM events. Essentially, CCN concentrations were derived from the measured SMPS size distributions, assuming a "relative" chemical composition guided by the AMS measurements. As stated in the main text, the maximum correlations, and maximum agreement between measured and calculated CCN concentration could be achieved by lowering the surface tension (σ) from 72 to 57 mN m^{-1} (for a NUM mode organic/sulphate composition similar to the accumulation mode).

However, given that the Kelvin effect is very strong over the NUM size ranges, there is always the possibility that closure may be explained by instrument uncertainty in measurements of aerosol size, aerosol concentration and/or aerosol chemical composition. Therefore, we varied the key parameters that could influence closure by the order of ± 20 % – 30 % to evaluate the extent to which the closure could be achieved without altering the surface tension.

Note that calculations in this section are based on AMS bulk chemical composition, not size segregated, because of difficulties deriving an accurate NUM mode composition for 10-minute time resolution data (see section 2.1 above). Therefore, NUM effective κ, used in these calculations, is actually larger than it likely was (e.g. 0.45 instead of 0.28) due to lower contribution from OM in the accumulation mode, which drives the bulk composition. The latter results in a smaller surface tension reduction required for the closure with CCN, e.g. 57 mN m^{-1} instead of 49 mN m^{-1} as stated in the main text. Therefore, smaller effective κ

would require even larger discrepancies to explain the closure than the ones presented below as lower effective κ results in even greater deviation from the 1:1 line in Figure 2(e).

First, we take the dataset for the whole campaign excluding the NUM and plot the variation of normalised root mean square error (N-RMSE) as a function of the deviation from the measured particle number concentration as determined by a possible instrument percentage uncertainty – i.e. 0% represents the actual measured value (of number concentration in this case), and the minimum in N-RMSE represents the best agreement between the measured and calculated CCN (Fig. S2.3.1 a). An N-RMSE of 0 corresponds to absolute closure). Each point contributing to the trend lines in Figure S2.3.1. constitute the statistical outcome of the N-RMSE associated with the scatter plot analysis of the dataset. An example of selected scatter plots is shown in Figure S2.3.2.
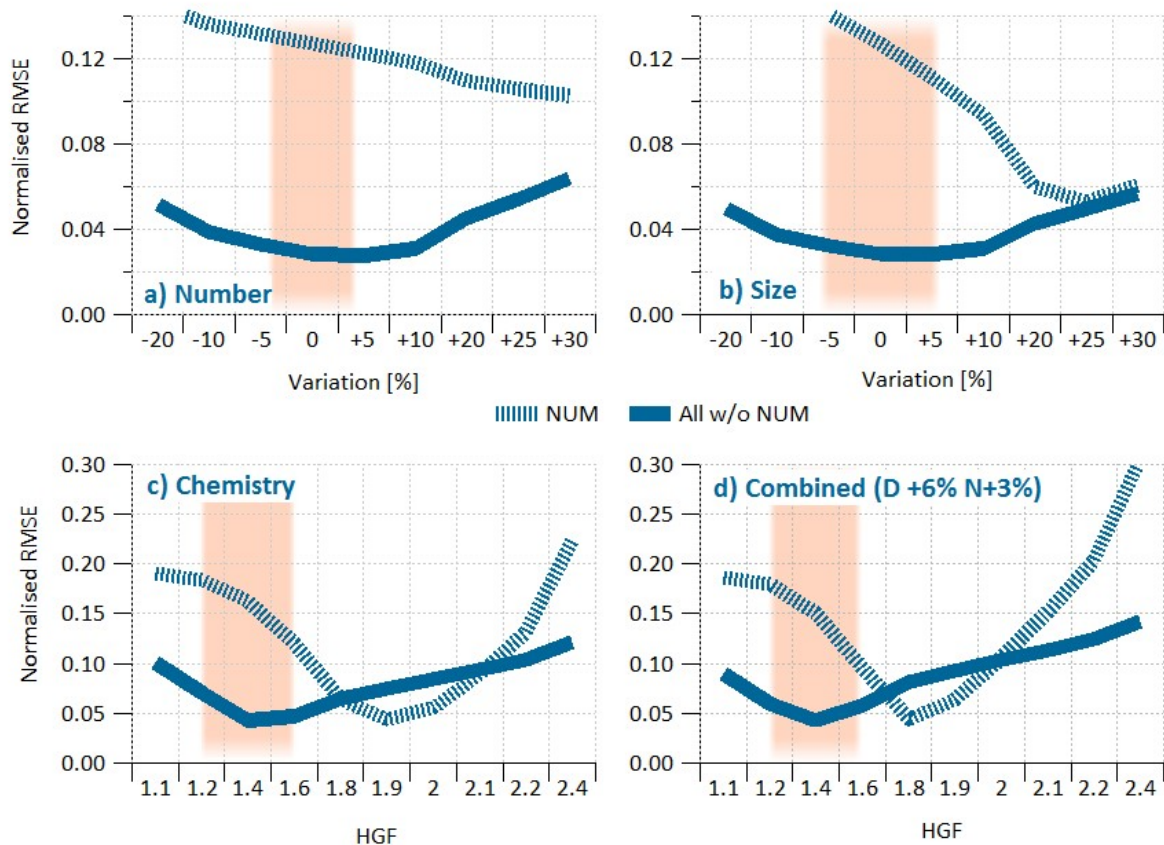
Figure S2.3.1. Sensitivity analysis of CCN calculations on measurement uncertainties of (a) number concentration, (b) particle size, (c) aerosol chemistry surrogate in the form of Hygroscopic Growth Factor (HGF) at 90% RH, and (d) a combined sensitivity of number, diameter and chemistry variation analysis (N-RMSE variation as a function of HGF including measured uncertainties of number and diameter, e.g. SMPS diameter amplified by 6% and number by 3%). The lines represent a change in the normalised (according to range) root mean square error (N-RMSE) with varying uncertainties in the measurements of number concentration, size,

HGF and combined. The variability for NUM events only, and all non-NUM data, is presented with dashed and solid lines, respectively. 0% variation corresponds to the CCN calculated concentrations derived from the actual measurements (i.e. SMPS diameter, number, etc). ±5%, ±10%, ±20%, +25%, +30% represent a potential percentage (%) over or under-estimation in size or number concentration. HGF is varied from 1.1 to 2.4. Note: Surface tension of 72 mN m^{-1} was used for number, size and chemistry sensitivity tests. The smaller the N-RMSE, the better is the agreement between measured and calculated CCN. The shaded areas in the a) and b) represent the calculated instrument measurement error; c) and d) HGF of typical NUM events.

For particle number concentration, the minimum N-RMSE is 0.029 for the non-event data and this N-RMSE increases to 0.051 and 0.064 for a -20% and +30% variations, respectively, from the actual measured instrumental value. The shaded area in Figure S2.3.1a represents the calculated instrument measurement error, which, in this case, is 3% as illustrated above. In contrast, for the NUM data, the N-RMSE decreases monotonically from 0.14 at -20% to 0.1 at +30%. While a lower N-RMSE occurs for large increases in number concentration (i.e. significant undercounting by the instrument), tending towards closure, this only occurs for concentration variations well outside the instrument uncertainty range (as illustrated in the shaded area). In addition, as there is a tendency towards closure for NUM data as the % variation increases, this only forces the non-event away from closure simultaneously. Consequently, we can rule out measurement uncertainty in particle number concentration as a potential contributor to the closure.

Similarly, the effect of % variation in aerosol size (derived from the SMPS) on N-RMSE is illustrated in Figure S2.3.1 b), along with the calculated instrument measurement uncertainty of 6% represented by the shaded area. The minimum in the N-RMSE for non-event data is 0.029 for 0% variation, with relative maxima for -20% and +30% of 0.05 and 0.06, respectively. For the NUM data, a steep fall off is also seen from 0.165 to 0.053 for -20% to +25%, respectively. Although under-estimation in size by 25% approaches closure, this again occurs well outside the uncertainty range for the measurement, reduces closure for the whole campaign (i.e. non-event data) and, consequently, cannot be a potential contributor to closure.
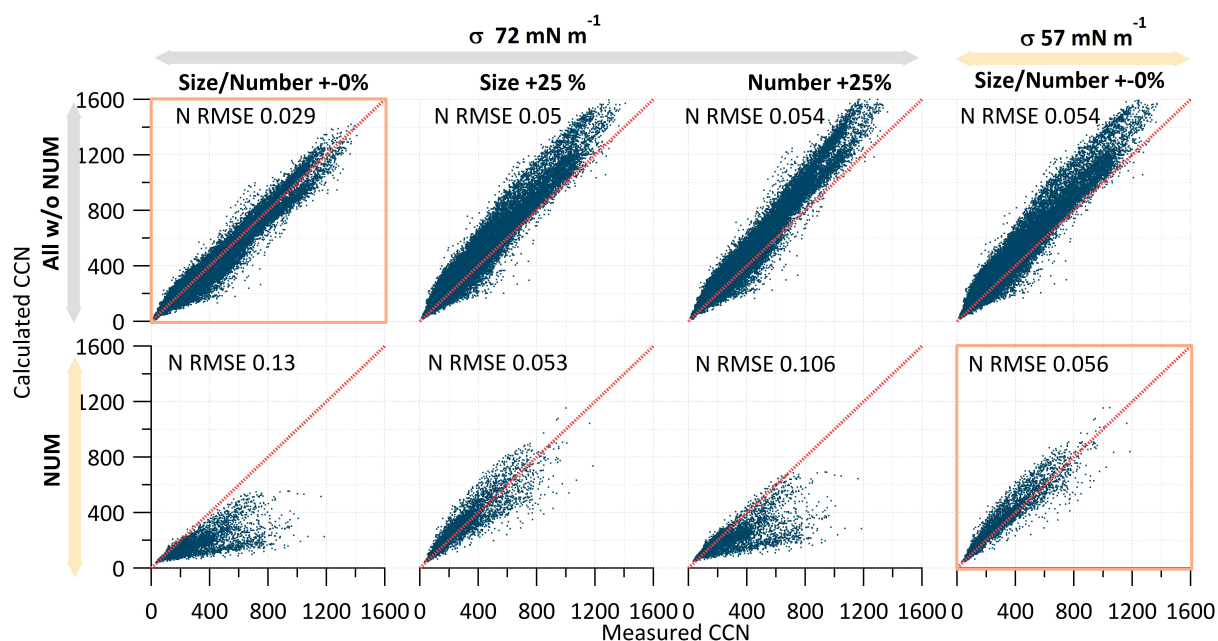
Figure S2.3.2. Scatter plots for calculated and measured CCN concentrations for original conditions and extreme deviations from the number, size and surface tension values.

In the sensitivity analysis for aerosol chemistry, we chose to encapsulate chemical composition and associated complexity into HGF (at 90 % RH) as this factor was used in the current manuscript CCN calculations *via* the *kappa (κ)* factor and represents the worst case scenario. As stated in the AMS uncertainty section, the accuracy of the AMS measurements is affected by the instruments collection efficiency, which would be the same for all compounds in the internally mixed particle. Thus, varying absolute AMS compound concentrations by any percentage would not have effect on the resulting relative contribution and, therefore, HGF derived from it (HGF would be the same for particles of the same relative composition, even though absolute values would be larger/smaller by some percentage, but to the same degree for all compounds). Therefore, varying the absolute concentrations of chemical compounds by the same percentage will not affect HGF uncertainty and varying HGF itself represents the largest chemical uncertainties possible. The range of HGFs spanned from 1.1, representing almost pure organic composition, to 2.4 corresponding to pure sea-salt. For non-event data, the closest to closure is achieved for a HGF of 1.4, while the closest to closure for NUM occurs for a HGF of 1.9. During typical NUM events[39], the HGF is between 1.2 and 1.6 (i.e. the shaded area on the graph), again suggesting closure can only be achieved for HGF values that are far too large. This corroborates the observations of the chemical composition by the AMS (i.e. 55% organic/ 45% sulphate by mass) as HGF values of 1.4 - 1.5 can be achieved for 52% OM and 48% ammonium sulphate by volume ratio (lower value) or 64% OM and 36% sulphuric acid (equivalent to 55%/45% by mass) (upper value), note, the difference in volume fractions for ammonium sulphate and sulphuric acid arose from adding ammonium mass to the

measured nss-sulphate mass. Moreover, as stated above, AMS percentage contribution can only be affected by the instruments precision, which is on the order of few percent so cannot result in HGF of 1.9, which would require 70 % discrepancy between the measured and necessary composition (85% of sulphuric acid and 15% of organics) to get a HGF (at 90 % RH) of 1.9; however, as noted below, the relevant effective hygroscopicity, κ_{CCN}, of sulphuric acid in ultrafine particles shows a relative decrease at supersaturation compared to κ_{HGF} at 90 % RH.

Another, hypothetical, option could be an 85% contribution from sea salt instead of sulphuric acid, but we deemed this option being not realistic: in addition to all arguments presented above for sulphuric acid that are also valid for the sea salt, e.g. resulting HGF would significantly exceed the one measured for similar events. We observe a total of 40 ng m^{-3} sea salt mass without sizing information; however, based on extensive knowledge of sea-salt mass contributions to different particle modes[46], we concluded that the contribution to the ultrafine mode was unlikely to host more than a couple of percent of the observed total submicron mass. Moreover, the closure with CCN would require an addition of 600 cm^{-3} sea salt particles, which has never been observed in the extensive range of sea salt studies[46]. The largest ever recorded sea salt concentration at Mace Head was 150 cm^{-3} detected during storm-force conditions of 25 m s^{-1} [47], and then, only a minor fraction of these being attributable to the NUM. Furthermore, this particular event, and the similar 'open ocean particle production events' only occur during high biological productivity blooms in the ocean's surface waters[33], as illustrated by high chlorophyll levels in Figure S1.1.1. Sea spray is a primary aerosol produced from bubble bursting processes and comprises both sea salt and primary organic matter (POM). During high biological activity, the sea spray becomes enriched in organics at the expense of sea salt leading to organic enrichment of submicron aerosol to the order of 95 %[48]. Moreover, the degree of enrichment increases with decreasing size, most likely leading to more than 95 % enrichment in the ultrafine mode. Thus, the likelihood of sea salt contributing significantly to the NUM, despite possibilities of hypothetical processes, is extremely low.

We have also investigated a possibility of other than organic/sulphuric acid/sea salt compounds being able to reproduce the similar effect. One of which could be iodine or iodine oxides as the traces of iodine were detected in the NUM mode, e.g. 41 nm dry particles that activate at a supersaturation of 0.5 % have an effective hygroscopicity κ value of $\kappa_{CCN} = 0.87$ (based on CCN activation rather than hygroscopic growth). This means that without any surface tension reduction effects, they need to be slightly more hygroscopic than pure sulphuric acid at water-supersaturation conditions. We note that according to model calculations by Petters and Kreidenweis[49], sulphuric acid has a CCN-relevant κ_{CCN} of ~0.9; however, that κ_{CCN} value is applicable only to aqueous sulphuric acid particles of relatively large dry diameter (> ~300 nm), as shown in Fig. S2.3.3. Figure S2.3.3 presents hygroscopic growth factor based κ values (κ_{HGF}) as well as κ_{CCN} values computed by the

Aerosol Inorganic-Organic Mixtures Functional groups Activity Coefficients (AIOMFAC) model[50,51] over the RH range from 85 % to above 100 % for a temperature of 298.15 K and assuming a constant $\sigma = 72$ mN m^{-1} for the calculations of κ_{CCN}. Note that the thermodynamic mole-fraction based water activity as a function of solute concentration, related to κ (see Eq. S3.1.3), is accurately represented by AIOMFAC for aqueous electrolyte solutions (see Zuend et al.[18,19]), leading to reliable predictions of κ_{HGF} below and above water saturation. Figure S2.3.3 shows that both κ_{HGF} and κ_{CCN} vary with particle dry diameter when related to equilibrium RH (or saturation ratio) of a solution droplet, especially when the ultrafine size range is concerned. In comparison to particles of 300 nm dry diameter, significantly lower κ_{CCN} values are predicted for smaller ultrafine particles of 50 nm and 41 nm diameter in the case of sulphuric acid or ammonium sulphate. Briefly, the size-dependence of κ_{CCN} arises because of two main reasons: (1) the single-parameter concept of the hygroscopicity parameter κ is not perfectly capable of accounting for true ion association/dissociation in aqueous solutions, which can vary considerably at high dilution (water activity close to 1.0); (2) the water activity of the solution corresponding to the critical supersaturation of a particle depends on dry diameter (shift of the supersaturation maxima of corresponding Köhler curves with dry diameter). For the dry diameter range of interest in this study, appropriate values are $\kappa_{CCN} \approx 0.7$ for sulphuric acid and $\kappa_{CCN} \approx 0.58$ for ammonium sulphate. The value for ammonium sulphate is relatively close to the calculated value of $\kappa_{CCN} \approx 0.61$ stated (without providing an applicable particle size range) by Petters and Kreidenweis[49].

Dry generated iodine oxide has a κ_{CCN} of 0.54[52], which is close to the κ value of a particle consisting of a 36/64 – mixture (by volume) of rather hygroscopic organics (say, $\kappa_{CCN} = 0.25$) and sulphuric acid ($\kappa_{CCN} \approx 0.7$), so that without any surface tension effects the iodine oxide will not provide the activation of the particle. In fact, if the dry particle contains 30 % (by volume) sulphuric acid, 30 % of the rather hygroscopic organic matter, and 40 % of substance "X", the effective κ value of "X" needs to be as high as 1.5 for a 41 nm particle to activate at a supersaturation of 0.5 % (again, without any surface tension lowering effects and in this example for a rather high organic hygroscopicity). Finding such a substance "X" in the marine boundary layer – or any other part of the atmosphere - is highly unlikely, to say the least.
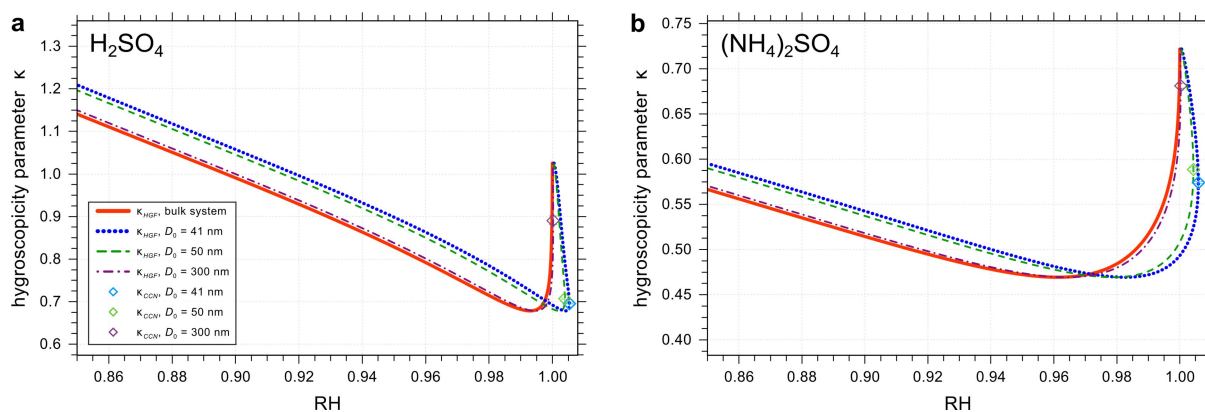
Figure S2.3.3. Hygroscopicity parameters κ_{HGF} and κ_{CCN} of (**a**) sulphuric acid and (**b**) ammonium sulphate, as predicted by the AIOMFAC model. All calculations are for T = 298.15 K and a constant surface tension of σ = 72 mN m^{-1}. The values of κ_{HGF} and κ_{CCN} at a particular relative humidity (RH) in equilibrium with an aqueous solution droplet depend on dry diameter (D_0). The predicted κ_{CCN} of sulphuric acid particles are: 0.695 for D_0 = 41 nm, 0.707 for D_0 = 50 nm, 0.766 for D_0 = 100 nm (not shown), and 0.891 for D_0 = 300 nm. The predicted κ_{CCN} of ammonium sulphate particles are: 0.574 for D_0 = 41 nm, 0. 589 for D_0 = 50 nm, 0.633 for D_0 = 100 nm (not shown), and 0.681 for D_0 = 300 nm. Error bars for κ_{CCN} symbols represent the uncertainty in the numerical resolution of the CCN activation point; uncertainty in RH is ~10^{-6}.

A combined sensitivity analysis was also performed to investigate whether the closure can be achieved by merging acceptable errors of multiple parameters, e.g. whether the minimum for N RMSE of HGF variation occurs at registered HGF values for NUM events when number concentration is increased by 3% and size by 6% (Fig. S2.3.1 d). 3% and 6% were chosen as maximum errors derived from the measurements and the direction (amplification by %) was derived from the N RMSE variation with number and size (a) and (b), accordingly: the closure is approached when N and D is increased and not vice versa. The N RMSE minimum was still at HGF values larger (1.8) than the HGF for NUM events (1.2-1.6) and the one arising from AMS uncertainty.

Surface tension sensitivity for NUM events and other than NUM time periods is presented in Fig. S2.3.4 surface tension of 57 mN m^{-1} that is suitable for NUM events (the minimum in RMSE) is not good for non-NUM events (RMSE increases from 0.028 at σ=72 mN m^{-1} to 0.053 at σ=57 mN m^{-1}), moreover, surface tension of 57 mN m^{-1} results in an overestimation of CCN (positive bias or almost all values residing above 1:1 line) for non-NUM event (top right panel in Figure S2.3.2). Therefore, a σ of 57 mN m^{-1} is valid only for the NUM events.

This analysis demonstrates that lack of closure for NUM events using a surface tension of pure water cannot be explained by uncertainties in the physico-chemical or water uptake measurements. Consequently, a lowering of σ to 57 mN m^{-1} leads to a minimum in the N-RMSE, while for non-events a surface tension of 72 mN m^{-1} leads to closure (Fig. S2.3.4).
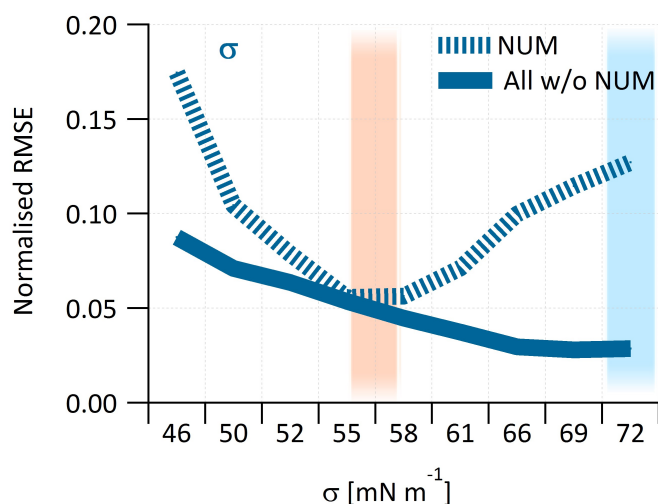
Figure S2.3.4. Sensitivity analysis of CCN calculations on surface tension variation. Surface tension is varied from 72 mN m^{-1} down to 46 mN m^{-1}. Red shaded area represents the surface tension of ~57 mN m^{-1} (used in the manuscript) and blue – the surface tension of 72 mN m^{-1} (water surface tension).

It is interesting to note that in a recent laboratory study, large oligomers of polyethylene glycol (PEG) were implicated in depressing the *SS** of mixed ammonium sulphate–PEG particles due to surface tension effects and non-ideal organic-inorganic interactions[53]. It is well known that oligomeric surfactants can possess greatly enhanced surface activity compared to the corresponding monomeric surfactants[54]. Whereas the AMS cannot establish conclusively the presence and structure of oligomers due to their fragmentation inside the instrument, we note that glyoxals and their oxidation products have been implicated as surface-active species[55,56]. It has also been reported[57] that glyoxal-derived oligomers lead to less-active CCN than the monomers; although, the extent to which the oligomer surrogates used in that study are representative of oligomers formed in the atmosphere is unclear

3 Thermodynamic modelling of particle growth: consideration of liquid-liquid phase separation and composition-dependent surface tension

In this section, we describe the general concept and applications of a state-of-the-art thermodynamic equilibrium model and its combination with a semi-empirical approach for composition-dependent surface tension for the prediction of particle growth. The main goals of this new approach are (i) to explore the hygroscopic growth properties and CCN activation behaviour of surrogate mixtures representing the observed NUM particles and (ii) to assess the interplay of non-ideal mixing, liquid-liquid phase separation (LLPS) and evolving surface tension on droplet growth at high relative humidity (RH).

In addition to the predictions by the comprehensive thermodynamic model, we also evaluate particle growth predictions by a simplified organic film model, inspired by the recent work by Ruehl et al.[58], and we discuss our results also in the context of their findings.

3.1 Köhler theory for hygroscopic growth

The hygroscopic growth of a particle under conditions of increasing environmental RH (or water vapour saturation ratio) is described by Köhler theory[59]. Equation (S3.1.1) is the commonly-used form of the Köhler equation that relates the equilibrium water vapour saturation ratio, S, over a spherical liquid solution droplet to its size and composition[49].

$$S = a_w \exp\left[\frac{4\,\sigma M_w}{RT\rho_w D}\right], \qquad\qquad (S3.1.1)$$

Here, D is the sphere-equivalent (wet) particle diameter at a certain equilibrium water vapour saturation ratio with respect to a curved aqueous solution droplet - or, in the case of a macroscopic (bulk) solution, mole fraction-based water activity, a_w. Note, $a_w = \text{RH} = S$ at vapour-liquid equilibrium for bulk solutions, i.e. for $D \to \infty$. σ denotes the effective air/particle surface tension at the droplet composition corresponding to size D, M_w is the molar mass of water, ρ_w the liquid-state density of water, R the universal gas constant, T the absolute temperature, and exp[…] the natural exponential function. The wet particle diameter can be related to a reference particle diameter at dry conditions, D_0; the ratio D/D_0 is known as the hygroscopic diameter growth factor (HGF).

In this study, Köhler theory is applied to predict the properties of particles of a certain dry diameter, e.g. for NUM particles with D_0 = 41 nm, either with (i) the surface tension fixed to the value of pure water (σ = 72 mN m^{-1} was used) or (ii) with a predicted, composition- and morphology-dependent (reduced) surface tension. The latter option is considered because the surface tension of actual particles depends on the surface composition and may therefore change with particle growth and actual molecular composition in a non-linear fashion[58], further discussed below.

We note that both the particle diameter and the water activity are functions of composition. In the case of a bulk system, in which interfacial energies between different liquid and/or solid phases and between the particle and the air (known as surface tension) are negligible, a_w is determined by the chemical composition only (mass or mole fractions of different mixture components). Thus, a_w constitutes the Raoult effect on droplet growth; however, its functional dependence on composition is non-trivial. We use a state-of-the-art thermodynamic equilibrium model to compute a_w (see Section 3.2). The particle diameter D is calculated by assuming linear additivity of the partial volume contributions by the mixture species based on their densities, as done in prior work[53,60]. Estimated pure-component densities for the surrogate systems studied in this work are listed in Tables S3.1 and S3.2.

In the context of κ-Köhler theory[49], the thermodynamic model allows for the prediction of the effective hygroscopicity parameter κ of the particle mixture at different water activities or saturation ratios. From Petters and Kreidenweis[49], the following expressions for κ are derived:

$$\kappa = 1 - (D/D_0)^3 + \frac{(D/D_0)^3 - 1}{S} \exp\left[\frac{4\,\sigma M_w}{RT\rho_w D}\right],$$ (S3.1.2)

$$\kappa = 1 - (D/D_0)^3 + \frac{(D/D_0)^3 - 1}{a_w} = [(D/D_0)^3 - 1]\left(\frac{1}{a_w} - 1\right).$$ (S3.1.3)

Equation (S3.1.2) can be used to determine values for κ from measured diameter growth factors at given S in the environment/instrument. Equation (S3.1.3) can be used with the thermodynamic bulk equilibrium model, which determines coupled value pairs (a_w and D) as a function of mixture composition (including consideration of a potential LLPS).

3.2   AIOMFAC-based thermodynamic equilibrium model

The growth of a particle with increasing RH is mainly due to the absorption of water vapour by partially or fully water-soluble aerosol components (hygroscopicity). Concomitant with water uptake, a secondary source of material for particle growth may be contributed by the gas-particle partitioning of semi-volatile organic compounds (and/or semi-volatile inorganic acids and bases) sensitive to the compositions of both the particle and gas phases[61]. Semi-volatile organic compounds with at least moderate affinity for water tend to exhibit enhanced partitioning to an aqueous phase accompanying an increasing water content as the particle equilibrates to a rising RH, also known as co-condensation, with potentially significant impact on particle growth and CCN activation[62,63]. The modelling approach introduced in this study includes the coupled equilibrium gas-particle partitioning of water and organic compounds to a bulk aerosol system. It therefore accounts for co-condensation effects on particle growth to the extent that such effects are represented by the volatilities of the selected system components, while neglecting potential competition effects on co-condensation in a dynamically growing particle population.

Thermodynamic equilibrium calculations were performed by application of a coupled LLPS and gas-particle partitioning framework[61,64] on the basis of activity coefficients computed by the Aerosol Inorganic-Organic Mixtures Functional groups Activity Coefficients (AIOMFAC) model[50,51]. The AIOMFAC model uses a group-contribution concept to describe the non-ideal mixing behaviour of multifunctional organic compounds, water and inorganic ions. Non-ideal mixing in a liquid solution is caused by (i) differences in the molecular shapes and sizes (the combinatorial effect on mixing entropy) and (ii) by differences in the energetic interactions among different kinds of molecules/ions. These two effects combined lead to deviations from ideal mixing. The deviations are accounted for by thermodynamic activity coefficients (here defined on mole fraction basis for water and organic compounds and on molality basis for inorganic ions)[50]. Liquid-liquid phase separation emerges as a

consequence of a substantial degree of non-ideal mixing to the point where the formation of an additional phase becomes thermodynamically favourable (stable liquid-liquid equilibrium state) in comparison to a single, homogenous liquid phase[61,65].

We note that in the presence of LLPS an additional interfacial energy contribution to the total Gibbs energy of a gas-particle system arises at the liquid-liquid interface. As is the case with surface tension, this interfacial energy contribution is negligible for bulk systems, yet may become significant in the case of tiny particles with relatively high surface/volume ratios. Consideration of interfacial energy contribution effects from liquid-liquid and liquid-air interfaces require a model for the interfacial energy per unit area of interface as a function of the chemical compositions of both liquid phases; this as part of a fully coupled, size- and LLPS-dependent equilibrium modelling approach. At this point, we make the simplifying assumption that the liquid-liquid interfacial energy contribution per unit area ("interfacial tension") is small compared to the surface tension and, as a first-order approximation, can be neglected. This assumption is supported by available measurements for organic-inorganic LLPS systems containing oxygenated organic compounds, which indicate that the liquid-liquid interfacial tension value is typically one to two orders of magnitude smaller than the surface tension (i.e., typically smaller than 10 mN m^{-1}, often smaller than 2 mN m^{-1})[66,67].

We acknowledge that ignoring the surface tension effect (i.e. the Gibbs energy contribution for forming a surface of a certain area and composition) during computations of the (bulk) equilibrium particle phase compositions may introduce an error, specifically when a significant fraction of the molecules resides at the particle surface (note: this is distinct from the use of σ within the Köhler equation). However, the consideration of LLPS limits this from being a large error, since rather hydrophobic molecules that produce a surfactant effect (reduced surface tension), will partition predominantly into an organic-rich phase located at the surface, thereby allowing our LLPS approach to largely capture the surfactant effect – at least under conditions where the droplet surface is completely coated by an organic-rich phase, as discussed below. Further work will be necessary for the development of a more sophisticated model that includes surface and liquid-liquid interfacial energy feedback on the phase compositions of small particles. Based on the classical thermodynamic theory of interfaces[68], it is expected that neglecting the surface tension effect on equilibrium composition will lead to an underestimation of the amount of organic material in an organic-rich phase under conditions where the organic-rich phase covers only a fraction of the droplet surface. Therefore, it is reasonable to assume that the current thermodynamic modelling approach will provide an approximate lower limit for the surface tension reduction effect by LLPS at high RH. Introduced in Section 3.5, we also consider the predictions from a simplified organic film model, which provides an

approximate upper limit on the expected reduction in surface tension and its effects on particle growth. Thus, the evaluation of hygroscopic growth predictions from both models will provide bounds on the expected surface tension effect.

3.3 Impact of phase separation on morphology and droplet growth

In an LLPS case, the chemical compositions of the co-existing phases may be substantially distinct (e.g., most organic material in an organic-rich, water-poor phase and most inorganic material in an aqueous phase) or the two phases may be of similar composition. Furthermore, the two phases may also be of similar or very different sizes (phase volumes), all depending on the overall composition[65]. This notion is important in the context of this study since it means that for a hygroscopic particle exhibiting LLPS near activation size, the aqueous phase likely comprises most of the condensed organic and inorganic material, while the organic-rich phase may be of relatively small volume.

The consideration of a potential LLPS state in the presence of organic compounds of rather low polarity (therefore low hydrophilicity) and inorganic ions dissolved in an aqueous phase (salting-out effect), allows for a physically-sound, predictive description of composition-dependent solubility of organics in the aqueous phase; the aqueous phase being mostly responsible for particle growth at high RH. No assumptions about the water-solubility of organic compounds have to be prescribed. Because a rather hydrophobic organic-rich phase tends to exhibit a lower air-liquid surface tension, theoretical considerations show that at thermodynamic equilibrium such a phase will always be located at the air-particle interface – rather than being located somewhere in the particle interior[68-70]. Therefore, the organic-rich phase will form a complete shell (core-shell morphology) or partial engulfing morphology on an aqueous inorganic-rich core phase. Consideration of this LLPS effect shows that a phase separation may have substantial impacts both on the Raoult effect as well as on the effective particle surface tension. Therefore, in the case of small droplets, the Kelvin and Raoult effects are not really independent factors in the Köhler equation.

Moreover, under continuing growth conditions, the organic-rich phase will eventually either disappear due to reaching sufficient solubility in the increasingly dilute aqueous phase – or it will reach a relatively small volume compared to the growing volume of the aqueous core phase, such that it becomes impossible to form a complete organic shell of at least molecular monolayer thickness covering an aqueous core phase. Under such conditions, the organic material may spread out as "molecular islands" at the surface of the core phase rather than forming a coherent, partial engulfing phase of monolayer thickness. The transition from a coherent phase ("organic film") to a spread out "gaseous" state on a 2-dimensional (2D) droplet surface can be modelled as a 2D phase transition, as described, e.g., by the compressed film model and its associated equation of state introduced by Ruehl et al.[58]. Our thermodynamic predictions of the compositions and volumes of coexisting

phases allow the computation of the minimum droplet size at which monolayer thickness of the organic-rich phase is reached and surface coverage becomes less than unity.

3.4   Modelling approach for effective surface tension

On a macroscopic level, at constant pressure p and temperature T, the surface tension of a solution represents the additional Gibbs energy (G) required per unit area (A) of surface formed (molecular surface monolayer), i.e. $\sigma = \left(\frac{\partial G}{\partial A}\right)_{p,T}$; SI units of J m^{-2} = N m^{-1}, e.g. ref[68].

From a microscopic view point, this represents a surface energy penalty as a consequence of the reduced intermolecular cohesive energy each molecule experiences at the droplet surface, because it is surrounded by fewer neighbouring molecules compared to a location in the interior of the droplet volume. A thermodynamic equilibrium state favours minimization of the system's Gibbs energy and therefore of the surface area necessary to contain a certain volume of liquid; hence, the spherical shape of tiny suspended liquid droplets. This also means that it is favourable for an aqueous solution droplet to maintain a surface composition enriched in molecules that contribute a relatively low surface energy per area occupied and jointly establish an effective surface tension that is lower than that of pure water[71] ($\sigma_w = 72$ mN m^{-1} at 298 K [72]). Typical values for the pure component liquid-state surface tensions of low-polarity to moderately polar multifunctional organic compounds range from ~20 to ~50 mN m^{-1} in the temperature range from 288 to 298 K[73]. For example, at 298 K, surface tensions of 37, 27, and 26 mN m^{-1} were measured for formic acid, acetic acid, and propionic acid, respectively[74]; ~35 mN m^{-1} was determined for adipic acid[75], ~32 mN m^{-1} for oleic acid[76] and a range of 20 to 30 mN m^{-1} was inferred for a mixture of multifunctional organic compounds from α-pinene oxidation[77]. For simplicity and in reasonable agreement with the measured range of pure-component surface tensions, we use an average value of $\sigma_{\mathrm{org}} = 30$ mN m^{-1} for all organic compounds considered.

It is well-known that the prediction of the effective surface tension of complex mixtures is a difficult task. All methods in use are of semi-empirical nature[73,78]. In this study, the effective surface tension of a droplet of a certain dry diameter is calculated using a semi-empirical approach and assumptions outlined in the following:

1) In the presence of a LLPS, an organic-rich phase (labelled phase β) will establish a complete or partial shell covering an aqueous, inorganic-rich core phase α (see Fig. 3c in the main text).

2) The surface tension of an individual liquid phase is here expressed as the volume-fraction-weighted mean of the pure-component surface tension values (σ_k), e.g. for phase alpha

$$\sigma_\alpha = \sum_k \varphi_{k,\alpha}\, \sigma_k, \tag{S3.4.1}$$

where $\varphi_{k,\alpha}$ is the volume fraction of component k in phase α (and $\sum_k \varphi_{k,\alpha} = 1$). Component volume fractions are computed based on the predicted molar phase compositions, known molar masses and liquid-state densities (assuming that the densities also apply reasonably well in the limiting case of relatively thin surface phases). For an LLPS case, this leads to distinct σ_α and σ_β values. Since phase α is a very dilute (water-rich) aqueous phase at high RH, the surface tension effect of dissolved ions is negligible and, for simplicity, σ_{ion} is assumed to be that of pure water. The value of σ_α is found to be close to σ_w, while the value of σ_β ranges between 30 to 40 mN m^{-1}, depending on the water content of the organic-rich phase.

3) If present, phase β must be at least of a certain minimum thickness, $\delta_{\beta,\text{min}}$, roughly corresponding to an average molecular monolayer thickness. The value of $\delta_{\beta,\text{min}}$ is an input parameter in our approach. Here, the assumed parameter range is $\delta_{\beta,\text{min}} = 0.16$ to 0.3 nm, similar to the lengths scale of one to two covalent carbon-carbon bonds or van der Waals radii of carbon and oxygen atoms[79].

4) For a LLPS case and the assumption of spherical particles of dry diameter D_0, the composition-dependent volumes of shell phase β and core phase α determine particle diameter D at a certain RH level. Together with a given minimum thickness $\delta_{\beta,\text{min}}$, these variables then determine the (maximum) surface area of phase α covered by phase β, i.e., whether complete ($c_\beta = 1$) or only partial coverage ($c_\beta < 1$) is possible. The surface coverage parameter, c_β, is

$$c_\beta = \min\left[\frac{V_\beta}{V_\delta},\ 1\right]. \tag{S3.4.2}$$

Here, V_β is the volume of phase β at diameter D and V_δ is the corresponding volume of a spherical shell of thickness $\delta_{\beta,\text{min}}$, calculated as

$$V_\delta = \frac{4}{3}\pi\left[\left(\frac{D}{2}\right)^3 - \left(\frac{D}{2} - \delta_{\beta,\text{min}}\right)^3\right]. \tag{S3.4.3}$$

5) For a LLPS case, the effective surface tension of the droplet is calculated as the surface-area-weighted mean of the composition-dependent surface tensions from both phases:

$$\sigma = \left(1 - c_\beta\right)\sigma_\alpha + c_\beta\,\sigma_\beta. \tag{S3.4.4}$$

6) The composition-dependent variable triplets (D, σ, a_w) are used in Eq. (S3.4.1) to calculate the equilibrium saturation ratio of the droplet over the covered size range. The critical supersaturation, $SS^* = (S^* - 1) \times 100\,\%$, is determined from the maximum in the equilibrium saturation ratio (S^*) during droplet growth; calculated using high numerical resolution at high RH. Corresponding to S^*, the critical wet diameter for CCN activation, D^*, is recorded.

The outlined approach is of predictive nature for any given organic-inorganic aerosol system. The level of accuracy of the model predictions for droplet growth will depend on the validity of the mentioned assumptions and on the degree of model sensitivity to input parameters. For the systems tested in this work, it turns out that the predictions are only slightly affected by the choice of mixing rule for the surface tension of each phase introduced in step (2), e.g. whether volume fractions or mass fractions are used. This is mainly because for systems exhibiting LLPS at high RH, the surface coverage parameter c_β exerts the primary control on the effective surface tension (via Eq. S3.4.4). Consequently, the most sensitive model parameter turns out to be the chosen minimum thickness $\delta_{\beta,\min}$, which directly affects c_β. The value of $\delta_{\beta,\min}$ is not precisely constrained and it is reasonable to assume that its value depends on the kind of molecular compounds present in phase β. For example, Ruehl et al.[77] and Ruehl and Wilson[80] report a decrease in inferred organic film thickness from experiments with particles formed during α-pinene ozonolysis when ozone concentrations increase. In this work, we perform sets of model predictions with two distinct values for $\delta_{\beta,\min}$, 0.16 nm and 0.3 nm, to characterize the impact of this parameter. The applied range in $\delta_{\beta,\min}$ is comparable to the values of an organic film thickness parameter (δ_{org}) reported by Ruehl et al.[58] for a single-parameter approximation of their compressed film model fitted to experimental droplet growth data of dicarboxylic acids and α-pinene secondary organic aerosol.

3.5 AIOMFAC-based simplified organic film model

Following the idea of an organic film coating an aqueous, salt-rich core phase, introduced by Ruehl et al.[58,77,80] to explain measured droplet growth behaviour of organic-inorganic mixtures by a simple model, we employ a similar predictive organic film model. Instead of computing the equilibrium liquid-liquid phase partitioning of organic compounds of limited water-solubility, the simplifying assumption is made that all organic material resides in an insoluble organic film adsorbed to an aqueous, salt-rich core phase. The organic film is assumed to be water-free and to coat the core phase completely up to the point where a minimum thickness δ_{org} (= $\delta_{\beta,\min}$ in our model) is reached. Hence, this simplified model resembles our more complex thermodynamic equilibrium model with LLPS – with two major differences: (1) no organic material is allowed to dissolve into the growing aqueous phase and (2) no water partitions to the organic film "phase" (i.e. ~a permanent and complete organic/inorganic LLPS).

In contrast to the simplified organic film model by Ruehl et al., which uses κ-Köhler theory to estimate the growth of aqueous core phase, we account for the water uptake into an aqueous inorganic phase by using the AIOMFAC-based gas-particle partitioning model. This eliminates any issues regarding the "correct" choice of a κ parameter that would apply both at sub- and supersaturated conditions, as discussed e.g. in Hodas et al.[53]. The effective

surface tension and critical supersaturation arising from this organic film assumption is calculated using the same procedure (Section 3.4) as for the more sophisticated LLPS model.

As mentioned in Section 3.2, it is expected that the predictions from the simplified organic film model provide an upper limit on the possible reduction in surface tension (for a given choice of $\delta_{\beta,\mathrm{min}}$). This is due to the fact that the organic film assumption entails that complete organic film coverage is maintained up to the largest physically possible droplet diameter, i.e. until monolayer thickness is reached even with all organic material adsorbed at the surface. For organic compounds that are poorly or only moderately hygroscopic, a slight reduction in the Raoult effect (since no water uptake by the organic film is considered) is outweighed by allowing the droplets to grow to relatively large sizes already at low supersaturations because of a reduced σ (given that $\sigma_{\mathrm{org}} < \sigma_{\mathrm{w}}$), such that the Kelvin effect is significantly diminished. This enables CCN activation at significantly lower supersaturations than expected for an assumption of a constant surface tension corresponding to the value of pure water; see the discussion by Ruehl et al.[58].

3.6 Surrogate systems for mixed organic-inorganic NUM particles

Two surrogate systems were introduced with the goal to represent the observed organic aerosol fraction in the NUM particles with mixtures of organic compounds that contain a range of functional groups expected to be present in the observed aerosol. The sets of surrogate species considered by systems 1 and 2 are characterized further below.

Since chemically-resolved measurements of molecular compounds in the ultrafine particles are not available (as usual), the set of specific surrogate compounds is somewhat arbitrary, but constrained by the measured average elemental composition of the organic aerosol fraction available. The ranges in elemental O:C and H:C ratios determined by the AMS instrument were O:C = 0.64 − 0.82 (± 30 % uncertainty) and H:C = 1.46 − 1.32, depending on the method of data evaluation. These elemental composition values represent an average over the whole aerosol population below ~1 μm diameter (submicron range); thus, they are dominated by the particle composition in the accumulation mode which contributes predominantly to the submicron aerosol mass. A specific quantification of the elemental composition of the NUM particles separately was not possible to the same level of accuracy, but the comparison of selected mass/charge (m/z) signals between the NUM and accumulation mode populations indicate that the average O:C ratio of the NUM particles may have been significantly lower. According to Aiken et al.[81], the organic aerosol signal at m/z 44 is highly correlated to the average organic O:C ratio (with some uncertainty) and halving the m/z 44 percentage contribution to organic mass would result in a similar reduction in O:C ratio. During the NUM event, the percentage contribution of m/z 44 to total mass for NUM particles is roughly half that of the accumulation mode, 6.2 % and 13.3 % for NUM and ACCU, respectively. Therefore, the average O:C ratio of the NUM population could potentially be as low as half of the total submicron O:C, ~0.3 to 0.4 (± 30 %

additional uncertainty). The two surrogate systems were therefore assigned distinct organic compositions, such that they represent average O:C ratios of 0.64 (system 1) or 0.43 (system 2).

The organic fraction in the particulate matter is mixed ~1:1 by dry mass with a sulphate-rich inorganic fraction, as suggested by the AMS spectra for the NUM. Either ammonium sulphate or sulphuric acid are used to represent the sulphate-rich inorganic fraction of the ultrafine particles and these inorganics were treated as non-volatile components. In the case of dissolved aqueous sulphuric acid, the dissociation equilibrium of bisulphate ions ($HSO_4^- \rightleftharpoons H^+ + SO_4^{2-}$) is considered by the thermodynamic model[50]. The model predictions suggest that the choice of sulphate species has a relatively minor effect on the resulting *SS**, such that some sets of model calculations were only performed with ammonium sulphate.

We acknowledge that actual marine aerosol likely contains a multitude of organic compounds in addition to those considered in our surrogate systems. We do not claim that our choice of components is perfectly representative of marine NUM particles; rather, the choice of compounds was guided by considering multifunctional aliphatic and aromatic compounds that include typical functional groups observed for marine secondary aerosol[82,83].

System 1. The first set of surrogate compounds is characteristic for secondary organic aerosol (SOA) components formed by the ozonolysis of α-pinene[64,84] combined with the organic compounds malic acid and phthalic acid, both found in marine aerosol[82], details provided below. The compounds of the mixture are listed in Table S3.1 together with information on mixture composition, densities and vapour pressures. The surrogate compounds span the range of volatilities from semi-volatile organic compounds (SVOC) to extremely low volatility compounds (ELVOC) under the present ambient conditions[64].

The resulting O:C and H:C ratios at 40 % RH for model system 1 are 0.64 and 1.46, respectively. As discussed above, this O:C ratio is therefore likely more representative of the average O:C of the accumulation mode particles and may by higher than expected for the NUM particles. In addition, during similar NUM events at Mace Head, hygroscopic diameter growth factors of mixed organic-inorganic particles were measured and HGF = 1.6 was typically determined at ~90 % RH. This HGF is in good agreement with the predicted bulk HGF of system 1 when ammonium sulphate is used for the inorganic fraction. From the total molar input composition given in Table S3.1, a particulate matter (PM) mass concentration of ~0.6 μg m^{-3} (~0.3 μg m^{-3} SOA) results, typical for a pristine air mass. Since system 1 contains a significant fraction of organic compounds in the semi-volatile and intermediate volatility range, some enhancement of the total PM mass concentration is predicted at high RH due to the co-condensation effect. The total molar concentration amounts of all semi-volatile species are assumed to partition to ultrafine as well as accumulation mode particles. This ensures that gas-particle equilibration by ultrafine particles is consistent with the

concentration of semi-volatile material in the gas phase, as constrained by the measured submicron particulate matter amounts and component volatilities. This is done because the equilibrium composition of particles depends on the total mass concentration of semi-volatile (and low-volatility) organic compounds in a coupled, non-linear way (see, e.g. ref. [64]).

System 2. A second system of SOA surrogate compounds, listed in Table S3.2, is used to represent a less oxidized ultrafine aerosol consisting of enhanced amounts of high-molar-mass compounds of extremely low volatility and low to moderate hydrophilicity (O:C = 0.368 for the dimer compounds). This aerosol system was designed to contain ~87 % by dry SOA mass of the multifunctional "ALDOL dimer" and "ESTER dimer" compounds, suggested to form by the ozonolysis of monoterpenes. Here these multifunctional dimers represent a more general class of ELVOCs of rather limited affinity for an aqueous phase; hence, predicted to be predominantly present in an organic-rich phase. While this system is highly enriched in ELVOCs, such an abundance of ELVOCs present in nascent ultrafine particles could be a quite reasonable and common feature, since ELVOCs are expected to play a crucial role in the formation and condensational growth of new particles[84-86]. For example, Ehn et al.[85] suggest that the formation and growth of nanoparticles in controlled laboratory chamber experiments depend both on the sulphuric acid vapour concentration, $[H_2SO_4]$, as well as the lumped ELVOC concentration, [ELVOC], scaling approximately linearly with $[ELVOC]^2 \times [H_2SO_4]$.

From the input composition given in Table S3.2, a total particulate matter mass concentration of ~0.6 µg m^{-3} (~ 0.3 µg m^{-3} SOA) results for the entire RH range. Since this system contains mostly low-volatility compounds, the co-condensation enhancement of liquid-phase organics at high RH is a very minor effect. We note that the composition of system 2 leads to an average elemental O:C ratio of the organic fraction of ~0.43, representative of a lower average organic O:C in the NUM particles in contrast to the accumulation mode; the H:C ratio is ~1.46.

3.7   Results and discussion of thermodynamic model predictions

16 main sets of model predictions with different configurations were carried out; six for surrogate system 1 and ten for surrogate system 2. Additional sets of calculations were carried out to assess the impacts of uncertainties in the measured organic to sulphate ratio and in estimated pure component vapour pressures on CCN activation properties, further discussed in Sections 3.7.6 and 3.7.7. The main goal of these sets of calculations is providing a basis for the assessment of different combinations of model setup and input parameters on the surface tension evolution and critical CCN activation properties predicted by both the equilibrium LLPS model and the simplified organic film model. The tested configurations include a choice among sulphuric acid or ammonium sulphate to represent the inorganic sulphate component and two distinct values for the monolayer thickness parameter $\delta_{\beta,min}$.

The configurations and resulting model predictions are summarized in Table S3.3. All model calculations were carried out at a temperature of 288.15 K (15 °C, typical for the ambient conditions during the NUM event). Table S3.3 also lists critical supersaturation and diameter values at cloud droplet activation predictions for the assumption of a constant surface tension of σ = 72 mN m^{-1}, providing a comparison to the methods with variable surface tension. This is insightful because for the evaluation of laboratory experimental data and in the context of applications of κ-Köhler theory, frequently a constant surface tension of 72 mN m^{-1} is assumed.

3.7.1   Surface tension reduction impact on critical CCN activation properties

In good qualitative agreement with the conclusions from Ruehl et al.[58], our results also show that a more realistic model, accounting for evolving surface tension with particle growth, will predict a significant increase in the critical diameter alongside a decrease in the critical supersaturation for activation. It is key to realize that even when the effective surface tension near the activation point is approaching 72 mN m^{-1} (e.g. for the case with a large D_0 of 175 nm), D^* and SS^* may be significantly different from D^*_{72} and SS^*_{72} (the values for constant σ = 72 mN m^{-1}), D^* being typically 50 % to 100 % larger and SS^* 10 % to 50 % lower than SS^*_{72}. This is due to the fact that the actual surface tension may be of significantly smaller magnitude at earlier stages in the droplet growth process, especially in the case of mixed organic-inorganic systems containing sparingly soluble organic compounds.

Predicted particle growth and phase composition properties of system 2 for the high-RH range, of interest in the context of CCN activation, are shown in Fig. 3 (main text). Additional results for this system in terms of mass concentrations and gas-particle partitioning effects are shown in Fig. S3.7.1 for the extended range from 0 % to 101 % RH. For example, panels (c, d, e) of Fig. S3.7.1 show that the organic compounds of system 2 are predominantly present in the liquid phases at all RH levels. Thus, the co-condensation effect at high RH provides in this case only a minor source of additional condensational growth by organics. While in the ambient air additional intermediate volatility compounds may be present that could contribute to the particle growth (and surface tension reduction), this model system shows that such effects are not necessary to explain the observed surface tension reduction, but this does not mean that they could not play a role for CCN activation under different conditions[63].
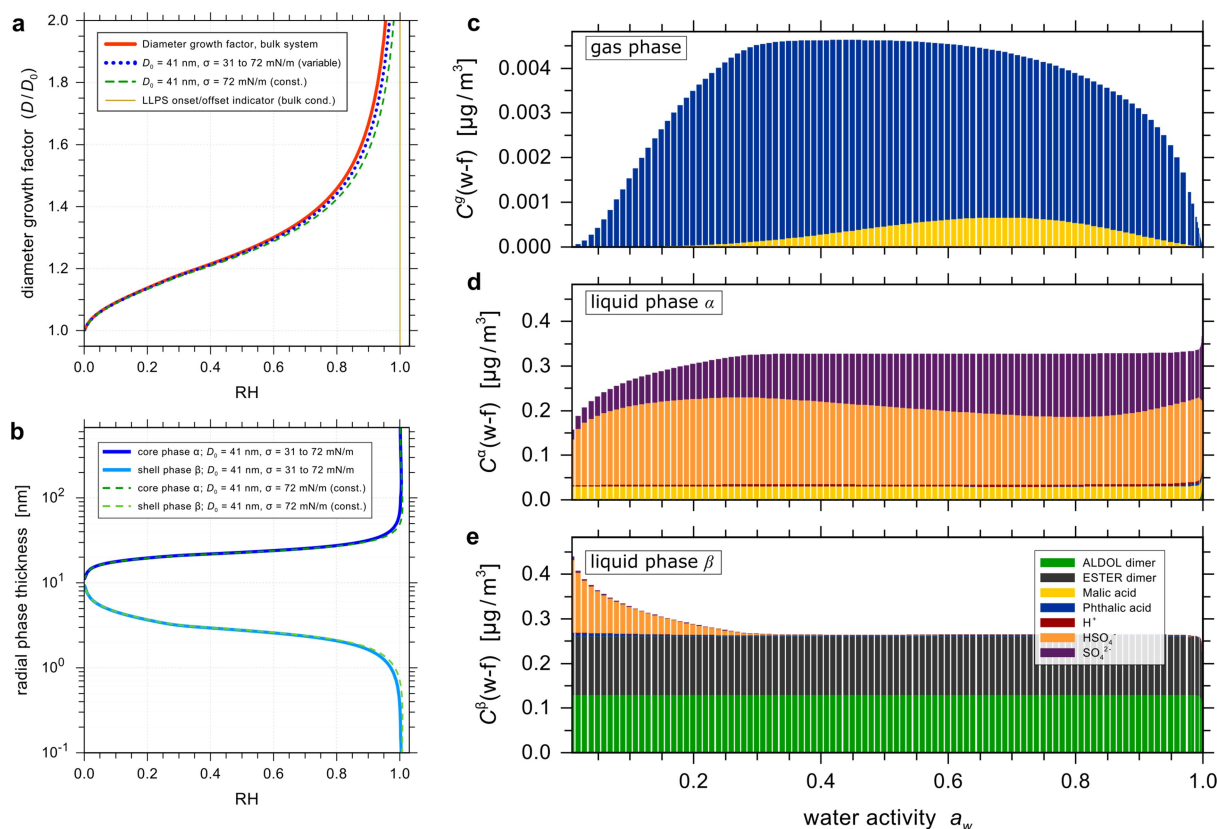
Figure S3.7.1. Thermodynamic equilibrium (LLPS) predictions for hygroscopic growth, radial phase thickness and phase compositions of the SOA plus sulphuric acid aerosol surrogate system 2, related to Fig. 3 of the main text, but showing system properties for the full RH range with $\delta_{\beta,min}$ = 0.16 nm. (a) Predicted diameter growth factors for the bulk system (red, solid) and the aerosol particles of dry diameter D_0 = 41 nm with evolving surface tension (blue, dotted) and constant surface tension of σ = 72 mN m^{-1} (green, dashed). The vertical yellow line marks the onset/offset of LLPS, here LLPS is present up to high RH beyond 100 % (see Fig. 3 of main text). (b) Radial thickness of the two liquid phases α, β. Phase α is considered the core and β the shell phase. Steep hygroscopic growth occurs at RH > 98 %. (c, d, e) Phase compositions shown for the dehydration case in terms of species mass concentration per m3 of air for the gas phase and the two liquid phases (on water-free basis). In this system, the enhanced partitioning of the semi-volatile compounds malic acid and phthalic acid from the gas phase to phase α at water activity levels above 98 % is only a minor contribution to the total aerosol mass concentration.

Compared to the surface tension of pure water, a mixed organic-inorganic particle's surface tension will be reduced most effectively in the presence of a LLPS with a core-shell particle morphology and a low surface tension of the shell phase β. The effective surface tension established by the composition of phase β will vary with changes in composition of that phase as a function of particle water content and organic gas-particle and liquid-liquid partitioning. It is important to note that the surface tension of phase β will only apply to the particle as a whole when phase β establishes a closed shell (full coating of phase α). We can assess whether this is possible by considering the actual thickness of shell phase β on a growing droplet prior to activation. For example, Fig. 3d quantifies that phase α is substantially larger in radius than phase β (as phase α establishes a spherical core), reaching

a diameter of ~311 nm at activation for D_0 = 41 nm. For the LLPS model, the radial thickness of shell phase β of this particle ranges from ~3 nm at 40 % RH (see Fig. S3.7.1) to 0.16 nm (assumed $\delta_{\beta,min}$) at ~100.272 % RH (corresponding to a_w = 0.99756). As the droplet grows further (while equilibrating to a rising supersaturation), the surface coverage, c_β, decreases (see Fig. 3b), which means that phase β likely establishes a partial engulfing LLPS morphology once monolayer coverage is no longer possible – or, alternatively, the organic constituents may spread out over the whole surface of phase α, establishing "islands" of surfactants (Fig. 3c) in what is also considered a 2D gaseous state from the perspective of a 2D phase transition in a compressed film approach[58].

In Fig. 3, the transition from a LLPS state to a single liquid phase is denoted by a vertical yellow line and, in case of the bar graphs, is also evident by the co-existence of two liquid phases of distinct compositions (panels e, f) up to a water activity of 0.9997. Note that the mole fraction-based water activity of a bulk solution at vapour-liquid equilibrium is equivalent to RH; however, for small particles, the water activity at a certain particle composition will always be lower than the equilibrium RH – this is a direct consequence of Köhler theory (Eq. S3.1.1). The existence of a LLPS up to high RH clearly indicates the presence of organic compounds of limited water solubility. Depending on the SOA mixture composition and particle dry size, these organic compounds will remain in a separate phase up to CCN activation size and in certain cases beyond that particle size, as shown in Figs. 3, S3.7.2, S3.7.3, S3.7.4 and by model predictions for a similar, but salt-free SOA system[87]. In other cases, where the phase separation does not persist up to supersaturated conditions, the hydrophobic organic compounds remain likely candidates for exhibiting enhanced partitioning from the droplet bulk to the surface layer at particle diameters close to CCN activation. This may be sufficient to suppress the surface tension to values significantly less than that of pure water[53].
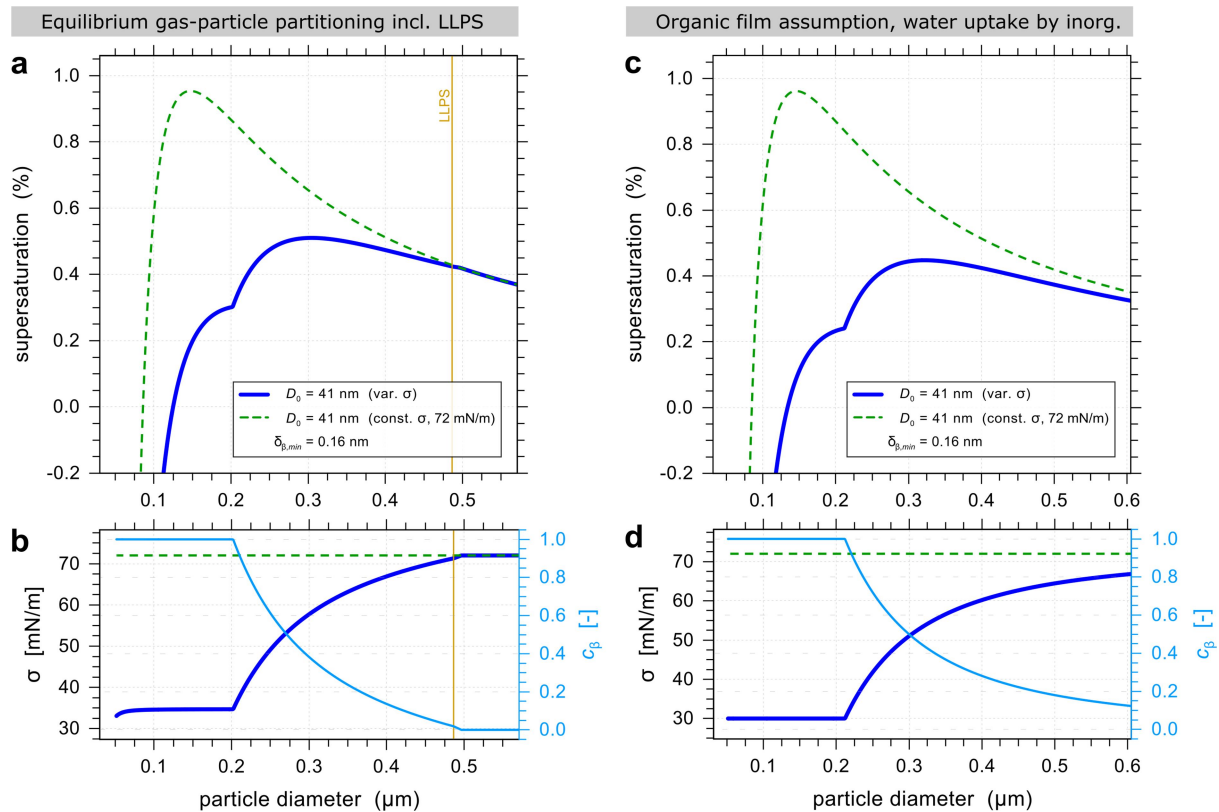
Figure S3.7.2. Particle growth model predictions at high RH close to CCN activation for surrogate system 2 with ammonium sulphate as inorganic component and for $D_0 = 41$ nm, $\delta_{\beta,min} = 0.16$ nm. All results are for a temperature of 288.15 K and an organic to ammonium sulphate mass ratio of ~1:1. (**a, b**) Köhler curves, effective surface tension, and surface coverage, c_β (light blue), as predicted by the equilibrium gas-particle partitioning model with consideration of LLPS (similar to Fig. 3a,b of main text). (**c, d**) Corresponding predictions obtained with the simplified organic film model. Note the reduced effective surface tension (blue curve) and associated reduced critical supersaturation with the organic film model, $SS^* = 0.45$, compared to (a), $SS^* = 0.51$, because all organic material is assumed to be adsorbed at the particle surface.

Figure 3a shows the prediction of the equilibrium supersaturation vs. particle diameter obtained from the thermodynamic equilibrium model with consideration of LLPS. As expected, a particle of 41 nm dry diameter with composition-dependent (reduced) surface tension, shown in Fig. 3b, is predicted to undergo CCN activation at a substantially lower supersaturation ($SS^* = 0.50$ %) and larger diameter ($D^* = 311$ nm) than a particle with an assumed constant surface tension at the pure water value ($SS^*_{72} = 0.88$ %, $D^*_{72} = 164$ nm), as clearly visible by the distinct locations of the global maxima of the Köhler curves. In addition, Table S3.3 lists also the critical properties for the same system composition and assumptions, but for the case where the simplified organic film model is used for the predictions, resulting in $SS^* = 0.43$ %, $D^* = 330$ nm. As discussed earlier, it is reasonable to assume that the AIOMFAC-based organic film model provides an upper bound for the surface tension reduction effect, thus, a lower bound for SS^*, while the AIOMFAC-based LLPS equilibrium partitioning model likely underestimates the surface tension reduction and, hence, provides an upper bound on the value of SS^*. Therefore, this case provides a proof-of-concept that aerosol particles of composition similar to system 2, with a critical

monolayer thickness of ~0.16 nm, are able to activate at a supersaturation of ~0.5 %, as observed during the conditions of the NUM event.
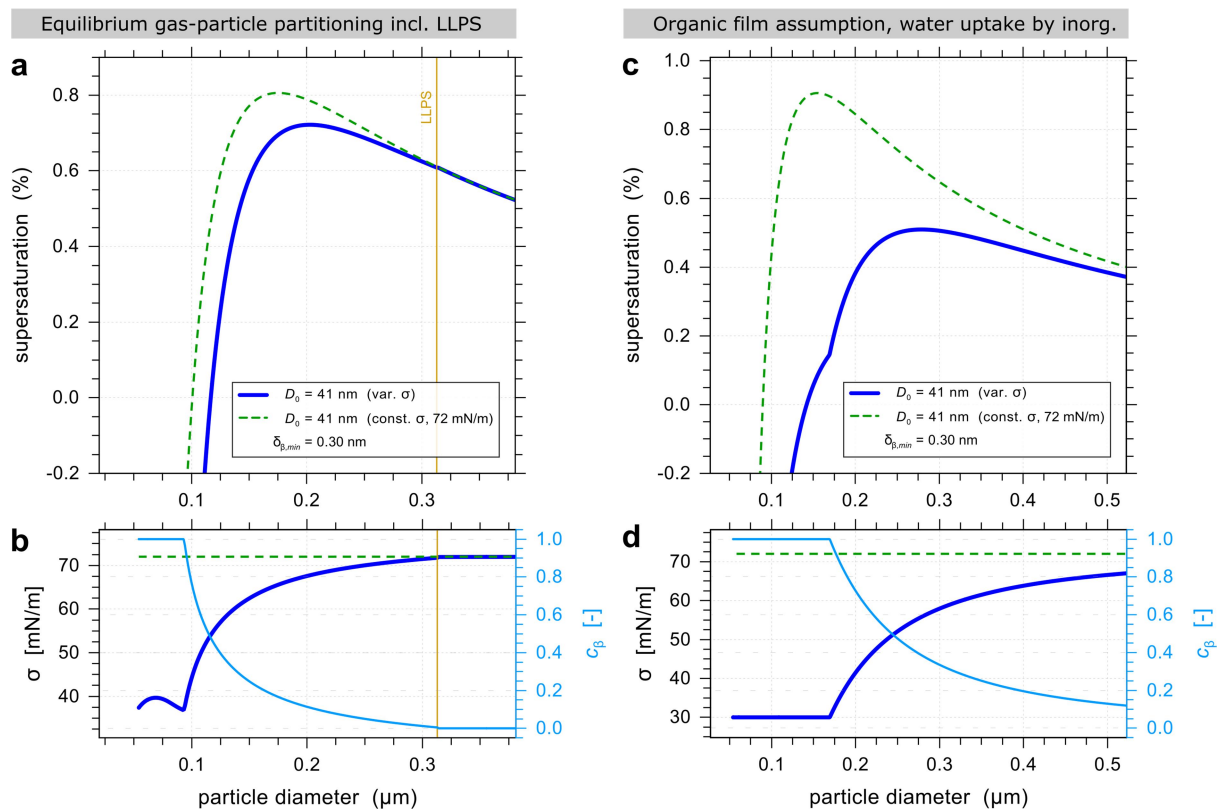

Figure S3.7.3. Particle growth model predictions at high RH close to CCN activation for surrogate system 1 with ammonium sulphate as inorganic component and for D_0 = 41 nm, $\delta_{\beta,min}$ = 0.3 nm. All results are for a temperature of 288.15 K and an organic to ammonium sulphate mass ratio of ~1:1. (**a**, **b**) Köhler curves, effective surface tension, and surface coverage, c_β (light blue), as predicted by the equilibrium gas-particle partitioning model with consideration of LLPS. This surrogate system has an average O:C ratio (0.64). In comparison to Fig. ST2, here the organics are more soluble in phase α, leading to a reduced volume of phase β. In combination with a higher threshold for the minimum thickness $\delta_{\beta,min}$, the resulting LLPS and surface tension effect on the critical supersaturation is decreased. (**c**, **d**) Corresponding predictions obtained with the simplified organic film model. Note that the organic film assumption leads to a much more pronounced reduction in SS^*. The dashed green curves differ between the two models, since hygroscopic water uptake in (c) is only due to ammonium sulphate.
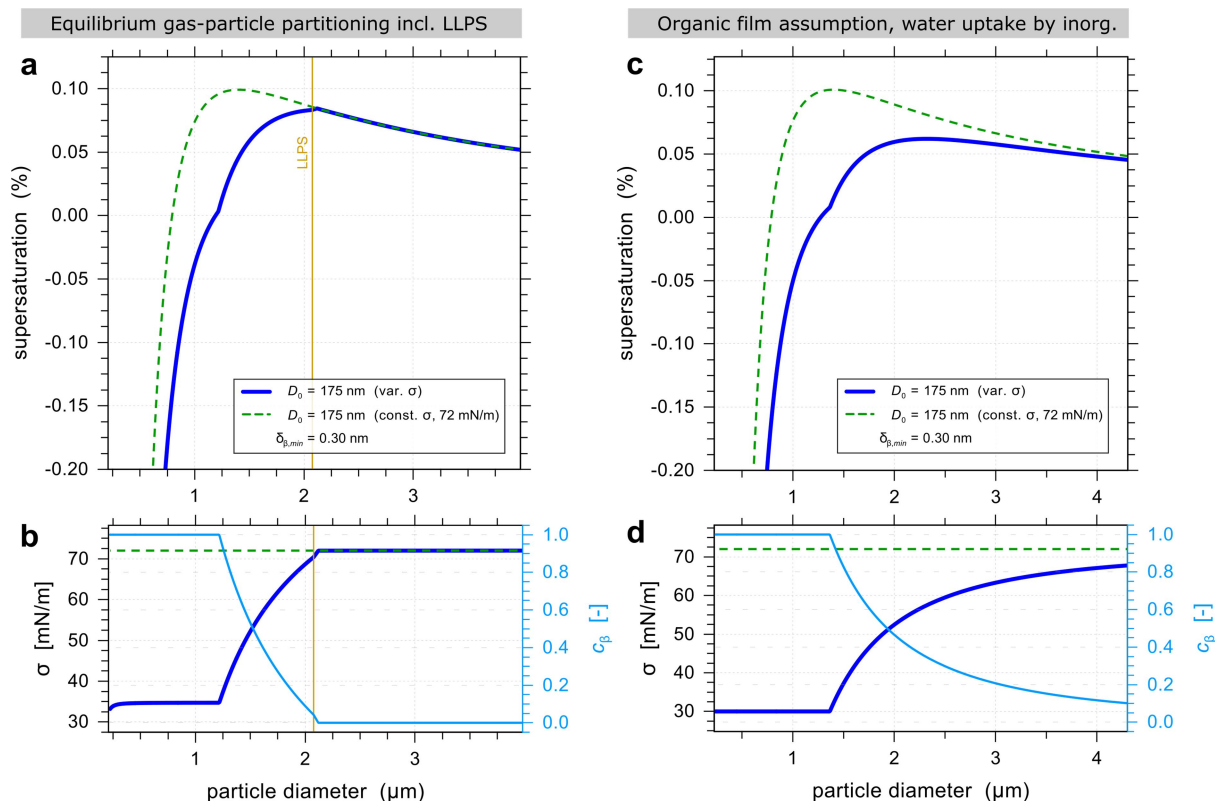
Figure S3.7.4. Particle growth model predictions at high RH for surrogate system 2 with ammonium sulphate as inorganic component. These predictions are for a relatively large D_0 = 175 nm and $\delta_{\beta,min}$ = 0.3 nm at a temperature of 288.15 K and an organic to ammonium sulphate dry mass ratio of ~1:1. (**a**, **b**) Köhler curves, effective surface tension, and surface coverage, c_β (light blue), as predicted by the equilibrium gas-particle partitioning model with consideration of LLPS. Note that for relatively large particles, in (a) the critical supersaturation for the case with variable effective surface tension (blue curve) is reached at conditions where σ = 72 mN m^{-1} and LLPS no longer exists – but at a larger D^* and lower SS^* than for the case with constant σ at all sizes (dashed green curve). (**c**, **d**) Corresponding predictions obtained with the simplified organic film model.

3.7.2 Impact of the choice of inorganic sulphate component

When using the same model configuration with system 2, but replacing sulphuric acid by ammonium sulphate, the predicted effect on SS^* is rather small; SS^* = 0.51 % for the LLPS model and SS^* = 0.45 % in the case of the organic film model (see Table S3.3 and Fig. S3.7.2). The Köhler curves and effective surface tensions for the two models are shown in Fig. S3.7.2. Additional comparisons of predictions over a wide range of organic to sulphate mass ratios are summarized in Table S3.4 and shown in Fig. S3.7.5 (discussed in Section 3.7.6). Those scenarios confirm that the choice of sulphate component has a minor impact on SS^*, with slightly smaller SS^* predicted when sulphuric acid is used. At first, the limited impact of choice of sulphate component might be surprising, because the inorganic contribution to hygroscopicity is expected to decrease when replacing sulphuric acid with ammonium sulphate. In fact, this reduction in hygroscopicity is noticeable when we compare the SS^*_{72}: 0.95 % for ammonium sulphate vs. 0.88 % for sulphuric acid (Fig. S3.7.2).

However, the impact is smaller when a concomitant surface tension reduction is considered, because a less hygroscopic core phase α will remain slightly smaller as low supersaturation levels are reached, which allows phase β to maintain a higher surface coverage up to higher supersaturations with a corresponding lower effective surface tension. Thus, the loss in hygroscopicity is effectively compensated for by a reduced surface tension, such that the resulting change in $SS*$ remains small. In conclusion, the choice of inorganic sulphate component has only a minor effect on the critical CCN activation properties.

3.7.3   Impact of monolayer thickness parameter

Table S3.3 also lists the model predictions for using the same configurations as above (system 2, with ammonium sulphate or sulphuric acid), but assuming a larger monolayer thickness of $\delta_{\beta,min}$ = 0.3 nm. Such a larger $\delta_{\beta,min}$ has the effect of decreasing the RH level / particle size up to which phase β may achieve complete surface coverage. Therefore, the surface tension reduction effect is diminished and activation will occur at a higher supersaturation. In the case of ammonium sulphate, the LLPS-related $SS*$ increases from 0.51 to 0.60 % while $D*$ decreases from 304 to 245 nm as $\delta_{\beta,min}$ is increased from 0.16 to 0.3 nm. For other cases, see Tables S3.3 and S3.4.

As discussed in Section 3.4, the $\delta_{\beta,min}$ parameter is one of the most sensitive model parameters, both for the equilibrium LLPS model as well as the simplified organic film model. Establishing improved physical/experimental constraints on this parameter in future will be valuable for predictive model applications.

3.7.4   Impact of organic system composition

The model predictions with surrogate system 1 show that larger differences in critical CCN properties are found when comparing the equilibrium LLPS model with the organic film assumption. For example, Fig. S3.7.3 shows the comparison of model predictions for system 1 with ammonium sulphate and $\delta_{\beta,min}$ = 0.3 nm. The volume of phase β is predicted to be relatively small (with the LLPS model), due to the presence of organics of higher average water-solubility in that system. This leads to a higher $SS*$ of 0.72 % compared to 0.60 % for the same conditions with surrogate system 2. In contrast, the organic film model ignores the higher solubility of the organics, maintains a higher surface coverage and therefore predicts a significantly lower $SS*$ of 0.51 %. Hence, according to a simple organic film model assumption, NUM particles of D_0 = 41 nm and system-1 composition would likely contribute to the fraction of activated CCN in a marine stratocumulus case. The main difference between surrogate systems 1 and 2 is that system 1 produces a higher average O:C ratio of ~0.64 in the condensed phase and it contains a larger fraction of semi-volatile organic compounds. Its chemical composition is likely more consistent with the observed accumulation mode particles, but not with the NUM population. Therefore, in qualitative agreement with the AMS measurements, which indicate a lower average O:C in the NUM, the LLPS-based model predictions suggest that particles of system-1 composition would

require a significantly larger dry diameter than 41 nm to activate at environmental supersaturations of 0.5 %.

The composition of the organic fraction of a surrogate system remains a key determinant in the context of surface tension reduction. With regard to particle hygroscopicity, the exact molecular structure of the organic compounds in a model system is likely of secondary importance, but the relative abundance of oxygenated functional groups, affecting the average O:C ratio and water-solubility of the organic fraction, is likely one of the key factors. The molecular structure (size, mass) of an individual organic compound with a certain O:C is, however, key with regard to its vapour pressure and other pure component properties.

3.7.5 Köhler curves for particles of larger dry diameters

The conclusions drawn from the evaluation of the predictions by the thermodynamic equilibrium LLPS model and the simplified organic film model are in good conceptual agreement with the findings from Ruehl et al.[58] and strengthen the evidence for surface tension reduction in mixed organic-inorganic aerosols. In this study, the focus was set on the growth and activation process for ultrafine particles, while Ruehl et al.[58] present experimental droplet growth data and model calculations for larger particles of dry diameters of ~150 nm and larger. For mixed organic-inorganic particles, e.g. SOA generated from α-pinene ozonolysis coated onto ammonium sulphate seed particles, Ruehl et al. state that droplet activation occurs once the mixed-particle's growth curve reaches the surface tension of pure water and intersects with the Köhler curve of the inorganic ammonium sulphate seed. This seems to be in contradiction with our findings, which suggest that activation occurs typically at surface tensions σ^* that are often significantly lower than the surface tension of pure water – and before the growth curve (blue curve in Figs. 3, S3.7.1 – S3.7.3) intersects with the Köhler curve for the constant $\sigma = \sigma_w = 72$ mN/m assumption. However, as shown in Fig. S3.7.4, this apparent contradiction can be dismissed by considering that the LLPS model predicts, at least qualitatively, the same behaviour for particles of larger dry size; here for $D_0 = 175$ nm, $\sigma^* = 72$ mN/m). Thus, from the differences in σ^* between ultrafine particles and larger accumulation mode particles, we conclude that droplet activation will not generally occur when $\sigma^* = \sigma_w$; rather, that finding by Ruehl et al. likely represents a special case that only applies to particles of larger dry size.

3.7.6 Sensitivity of critical supersaturation to organic/sulphate mass ratio

The thermodynamic model calculations summarized in Table S3.3 were carried out for an organic to inorganic dry mass ratio (OIR) of ~1. In terms of organic matter to sulphate dry mass ratio, an OIR of 1.0 leads to $OM/SO_4^{2-} \approx 1.03$ in the case of H_2SO_4 chosen as the sulphate component and to $OM/SO_4^{2-} \approx 1.38$ when ammonium sulphate is the inorganic sulphate component. Here we present a set of calculations showing that the predicted SS^* values are only weakly dependent on the OM/SO_4^{2-} ratio in NUM particles as represented by

surrogate system 2. Based on an uncertainty of up to ±20 % in the dry particle mass fraction of organic matter (OM), centred around 55 % OM, calculations were performed in particular for OM/SO_4^{2-} = 44/56 (≈ 0.786) and OM/SO_4^{2-} = 66/34 (≈ 1.941) in order to analyse how the critical supersaturation and other predicted properties vary as a function of dry particle composition within a reasonable range. The predictions for the key CCN activation properties by the equilibrium gas-particle partitioning model with LLPS and the simplified organic film model are summarized in Table S3.4. The corresponding model input compositions are given in Table S3.5.
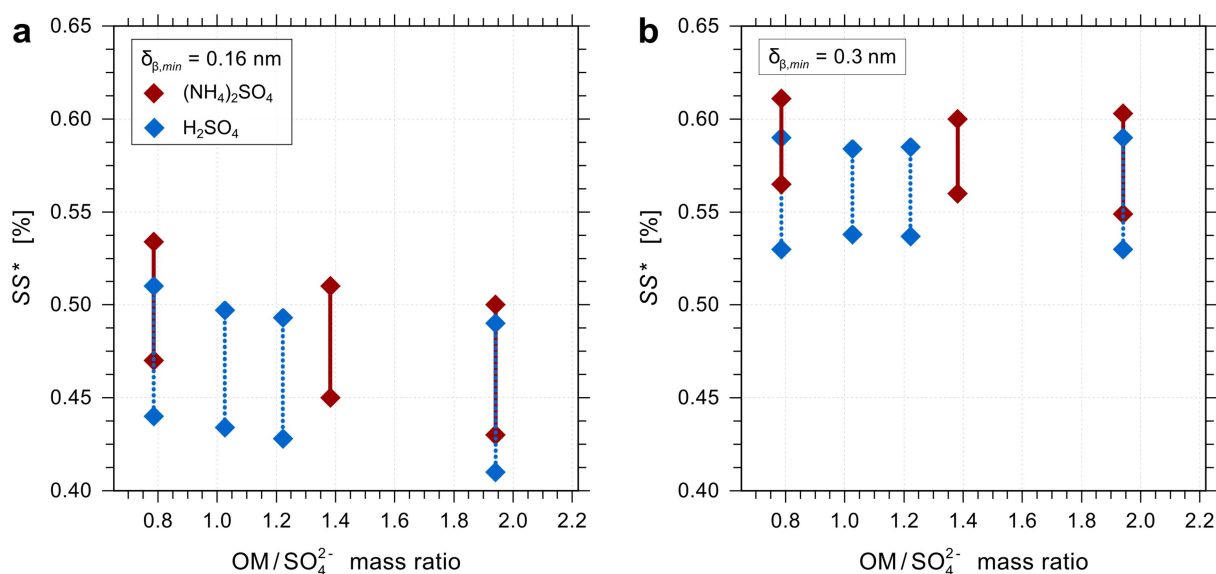

Figure S3.7.5. Model predictions of the critical supersaturation (SS^*) for different organic matter (OM) to sulphate dry mass ratios in the range OM/SO_4^{2-} = 44/56 to 66/34. The predictions are for surrogate system 2 at a temperature of 288.15 K, for D_0 = 41 nm and for (**a**) $\delta_{\beta,min}$ = 0.16 nm or (**b**) $\delta_{\beta,min}$ = 0.3 nm. The inorganic sulphate compound is either ammonium sulphate (red, solid) or sulphuric acid (blue, dotted). For each connected pair of points, the symbol at the higher SS^* value denotes the prediction by the equilibrium gas-particle partitioning model with consideration of LLPS, while the lower SS^* value marks the prediction by the simplified organic film model (see also related data in Tables S3.3, S3.4 and S3.7).

Figure S3.7.5 shows the effect of variations in OM/SO_4^{2-} on the predicted SS^* for NUM particles of D_0 = 41 nm and with parameter $\delta_{\beta,min}$ = 0.16 nm or $\delta_{\beta,min}$ = 0.3 nm. For each OM/SO_4^{2-} ratio and choice of sulphate-containing compound, two values for SS^* are obtained from the two models. As discussed in Section 3.2, the two models are expected to provide upper and lower limits for SS^* for systems with liquid-liquid phase separation at high RH. The model predictions demonstrate that SS^* varies only weakly within the shown OM/SO_4^{2-} range for a given $\delta_{\beta,min}$ parameter. Overall, the choice of characteristic monolayer thickness parameter $\delta_{\beta,min}$ is more influential. For the cases with $\delta_{\beta,min}$ = 0.16 nm, a slight

decrease of SS^* is predicted with an increase in OM/SO_4^{2-}, both for ammonium sulphate and sulphuric acid, with sulphuric acid also leading to slightly lower SS^* values in comparison to ammonium sulphate. These results suggest that a decrease in sulphate content, and therefore overall particle hygroscopicity, is at least compensated for by a prolonged surface tension lowering (to larger diameters during humidification) due to a larger relative amount of organic matter present. Exploring this effect to even higher or lower OM/SO_4^{2-} (beyond the estimated uncertainty of the NUM composition in terms of OM/SO_4^{2-}), e.g. for a dry mass ratio of 85/15 ($\approx$ 5.67), with sulphuric acid and $\delta_{\beta,min}$ = 0.16 nm, the two models predict upper and lower values for SS^* of 0.50 % and 0.44 %, respectively, indicating that this balancing effect between hygroscopicity and surface tension reduction is maintained to quite high OM/SO_4^{2-}. For an analogous case, except for an OM/SO_4^{2-} dry mass ratio of 15/85 ($\approx$ 0.176) enriched in sulphate, the predicted upper and lower values for SS^* are 0.55 % and 0.50 %, respectively (Table S3.4). Note that such a balancing effect over a wide range in OM/SO_4^{2-} is nontrivial; it is expected to be absent in cases where the evolution of surface tension during particle growth is ignored (i.e. when a classical κ-Köhler model is used). This is also seen from the predicted variation of SS^*_{72} with OM/SO_4^2, since that quantity captures the relative loss in hygroscopicity with increase in OM/SO_4^{2-}. For example in the cases with sulphuric acid and $\delta_{\beta,min}$ = 0.16 nm, the SS^*_{72} value predicted by the LLPS model increases from 0.64 % at a high sulphate fraction of OM/SO_4^{2-} = 15/85 to 0.82 % at 44/56 and further to 1.50 % at OM/SO_4^{2-} = 85/15, i.e. an absolute change of +0.86 % in SS^*_{72} (see Table S3.4). In contrast, when the evolving surface tension reduction by the organics is considered, the predicted SS^* value changes only by -0.05 % SS^* over the same range in OM/SO_4^{2-}. In general, the magnitude of the balancing effect will also depend on the hygroscopicity, water-solubility and abundance of organic compounds present in internally-mixed aerosol.

In conclusion, the predicted SS^* value ranges from both models indicate clearly that SS^* is rather insensitive to relatively large variations in OM/SO_4^{2-} (at least for particle mixtures similar to surrogate system 2), which would not be the case if the surface tension lowering effect and its evolution during particle growth were ignored.

3.7.7   Impact of uncertainties in pure component vapour pressures

Equilibrium gas-particle partitioning predictions on the basis of vapour-liquid equilibrium generally depend on the volatilities of involved components in a non-linear manner, in particular when semi-volatile organic compounds are abundant, see e.g.[61,88]. Therefore, the pure component liquid-state vapour pressures ($p°$) of the different system components are key parameters. Measurements of the relatively low $p°$ of semi-volatile and low-volatility organic compounds at atmospheric temperatures of relevance for aerosols are scarce and subject to a number of technical challenges[89]. In certain cases of organic compounds with multiple oxygen-bearing functionalities, measurements with different techniques have resulted in significantly different vapour pressures, sometimes deviating from each other by more than two orders of magnitude[89,90]. Semi-empirical estimation methods for $p°$ based on

chemical structure information are therefore frequently used, including for the organic compounds used in this study. Assessments of different vapour pressure estimation methods have shown that there are typically significant differences in predicted values for the relatively low-volatility compounds of interest here[91,92]. In a recent, comprehensive study, O'Meara et al.[92] assessed the seven most important $p°$ estimation methods (for applications in atmospheric science) against available measurements and also evaluated their impact on predictions of organic aerosol mass concentrations. The EVAPORATION model by Compernolle et al.[93] was found to be among the best methods, in particular for subsets of relatively low-volatility compounds, for which some other techniques tend to show large deviations from experimental data. EVAPORATION is the standard $p°$ estimation method used in this study and is considered to provide reasonably good estimates. However, uncertainties on the order of a factor of ten or more in the predicted $p°$ values exist, especially in the case of the ELVOC compounds, due to a lack of experimental data for such compounds (and therefore a lack of proper model validation).

In order to provide a quantitative comparison for the sensitivity of our model predictions with respect to $p°$ values, we provide here a case comparison with three distinct $p°$ estimation methods: (i) EVAPORATION, (ii) the method of Nannoolal et al.[94] with normal boiling point temperatures (T_b) estimated by the model of Nannoolal et al.[95] (denoted in the following as N-N method) and (iii) the method by Myrdal and Yalkowsky[96] with T_b estimation by the model of Nannoolal et al.[95] (denoted in the following as MY-N method). As noted by O'Meara et al.[92], the EVAPORATION and N-N methods are typically better suited for predictions of $p°$ of low volatility compounds, while the MY-N method has been shown to have a high bias in the predicted $p°$ of low volatility compounds. Here the application of MY-N serves the purpose of setting an upper limit in expected $p°$ in comparison to the prediction by EVAPORATION (considered more accurate), thereby representing a large uncertainty range. The three methods were applied to the organic components of surrogate system 2, with the values listed in Table S3.6. The $p°$ predictions by EVAPORATION and N-N agree within a factor of 10 or better, while the values by MY-N are clearly higher compared to the other two methods, especially for the ELVOC compounds, for which deviations by up to four orders of magnitude in predicted $p°$ result.

Each vapour pressure prediction method was used separately within the gas-particle partitioning model to produce corresponding total molar input concentrations (n^t, gas + particle phase molar amounts of each component per unit volume of air) for a given particle composition at dry conditions (here at RH ≈ 10 %), given in Table S3.6. This is done because for our thermodynamic model calculations, the cumulative particle phase amounts are constrained (within uncertainty) by the field measurements, yet the gas phase amounts in equilibrium with these particle phase concentrations need to be determined to establish the total concentrations present per unit volume of air. Thus, this leads to a normalisation effect with higher gas phase amounts and therefore higher n^t predicted when the MY-N method is

used in comparison to EVAPORATION and N-N. The determined n^t values are then used in the gas-particle partitioning calculations as function of RH for the CCN activation predictions. Table S3.7 shows the critical CCN property predictions for system 2 with sulphuric acid and OM/SO_4^{2-} = 55/45. Mainly because of the mentioned n^t input normalisation, the three $p°$ methods applied yield similar critical supersaturation properties for 41 nm particles, as seen from the $SS*$ and $D*$ values listed in Table S3.7. For example, for $\delta_{\beta,min}$ = 0.16 nm, EVAPORATION and N-N lead both to $SS*$ = 0.49 %, while using the MY-N method results in $SS*$ = 0.53 %, i.e. an absolute change of only +0.04 % $SS*$ (see Fig. S3.7.6). It is interesting to note that the higher vapour pressures and larger n^t predicted by the MY-N method lead to a higher predicted organic matter concentration residing in the gas phase at intermediate RH levels, which may contribute to organic co-condensation and a droplet size enhancement effect at high RH (or higher water activity, see Fig. S3.7.6). However, the results for the cases here suggest that this co-condensation effect (which is accounted for in our model) is not substantial enough to lead to a lowering of the $SS*$ in this case in comparison to the use of EVAPORATION. A main reason for this result is a shift in the predicted effective surface tension to slightly higher values at lower particle diameters – caused by the enhanced partitioning of the moderately hygroscopic organic compounds from the gas to the particle phase α at RH above 95 %, which increases the overall particle diameter but at the same time reduces the surface coverage by phase β. This is seen in Fig. S3.7.6 when comparing the predicted effective surface tensions at a particle diameter of, e.g., 0.2 μm for the predictions with the EVAPORATION method (Fig. S3.7.6b) and the MY-N method (Fig. S3.7.6e).

In conclusion, the impact of existing uncertainties in the predicted pure component vapour pressures have only a very minor effect on predicted $SS*$, mainly because of the normalisation effect on applied input concentrations. The use of the EVAPORATION method with the equilibrium gas-particle partitioning model as the standard $p°$ method is therefore justified.
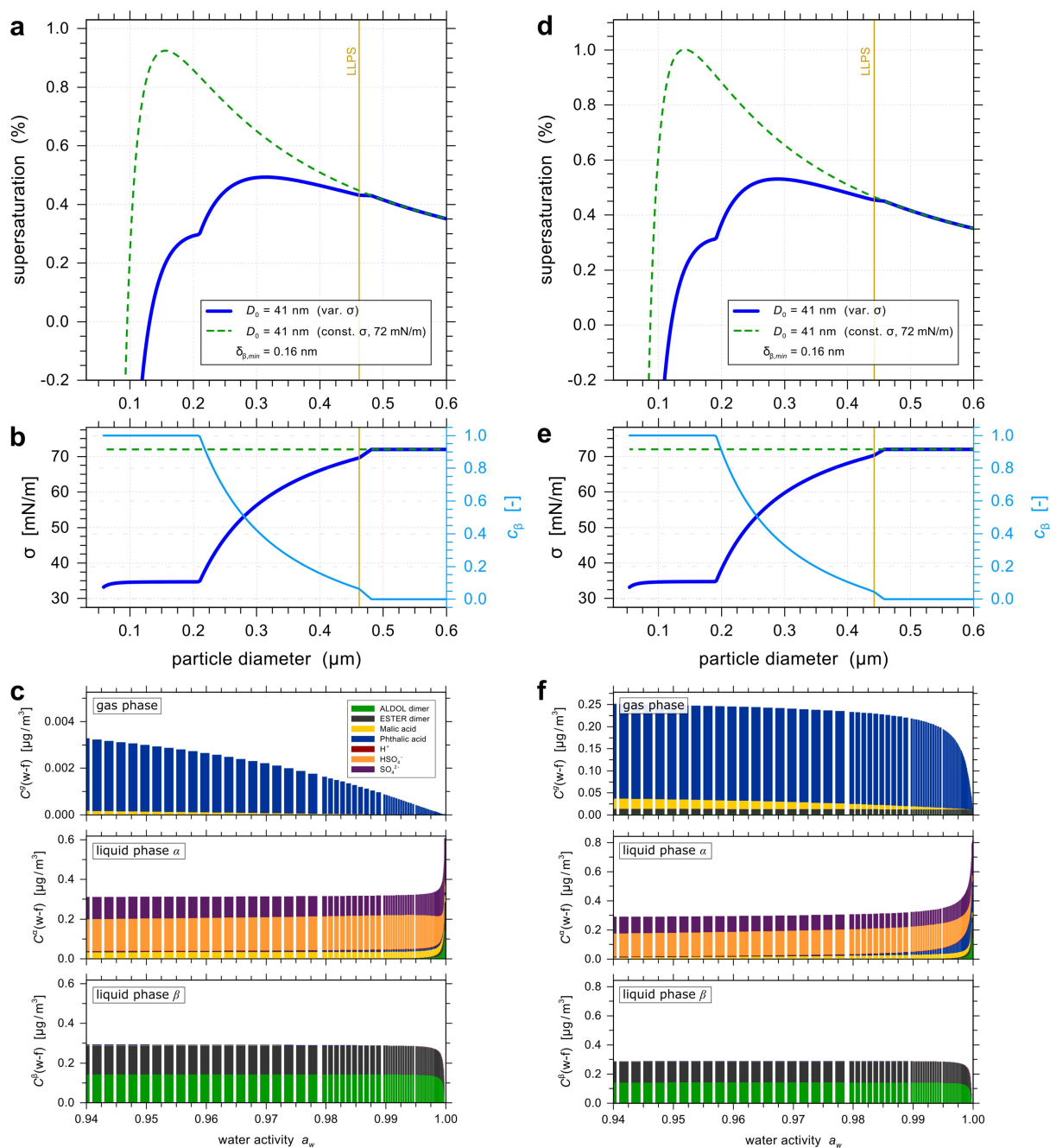
Figure S3.7.6. Equilibrium gas-particle partitioning (LLPS) predictions for surrogate system 2 with distinct pure component vapour pressures using: (**a**, **b**, **c**) the EVAPORATION method and (**d**, **e**, **f**) the Myrdal-Yalkowsky (MY-N) method (see also Tables S3.6, S3.7). All calculations are at T = 288.15 K, OM/SO$_4^{2-}$ = 55/45 and with particle growth parameters D_0 = 41 nm, $\delta_{\beta,min}$ = 0.16 nm. (a, d) Köhler curves, (b, e) effective surface tension, and surface coverage. (c, f) Component mass concentrations in gas and liquid particle phases (excluding water) vs. water activity in the range from a_w = 0.94 to ~1.0. Note the distinct ordinate axis scales and higher organic mass concentrations in the gas phase (f) when the MY-N method is used.

Table S3.1. Molecular properties and system composition of the set of SOA surrogates, water and ammonium sulphate or sulphuric acid, used for the thermodynamic equilibrium model calculations.

Name [a]	Molecular structure (SMILES)	O:C	H:C	p° [Pa] at T = 288.15 K [b]	Density [c] [g cm^{-3}]	n^{t} [d] [mol m^{-3}]
Water	[H]O[H]	-	-	1.706E+03 [e]	0.9971	RH-dependent
C107OOH	O=CCC1CC(OO)(C(=O)C)C1(C)C	0.400	1.700	3.092E-03	1.0922	4.564E-10
PINONIC	OC(=O)CC1CC(C(=O)C)C1(C)C	0.300	1.600	3.939E-03	1.0528	3.371E-10
C97OOH	OCC1CC(OO)(C(=O)C)C1(C)C	0.444	1.778	1.884E-04	1.1652	1.921E-10
C108OOH	O=CCC(CC(=O)C(=O)C)C(C)(C)OO	0.500	1.600	4.109E-04	1.0342	9.505E-11
C89CO2H	O=CCC1CC(C(=O)O)C1(C)C	0.333	1.556	1.286E-02	1.0750	1.494E-10
PINIC	OC(=O)CC1CC(C(=O)O)C1(C)C	0.444	1.556	8.813E-06	1.2103	4.367E-11
C921OOH	OCC(=O)C1(OO)CC(CO)C1(C)C	0.556	1.778	5.878E-07	1.2068	1.260E-10
C109OOH	OOCC(=O)C1CC(CC=O)C1(C)C	0.400	1.600	4.040E-03	1.0922	3.650E-11
C812OOH	OCC1CC(OO)(C(=O)O)C1(C)C	0.625	1.750	1.171E-07	1.2363	2.618E-10
HOPINONIC	OCC(=O)C1CC(CC(=O)O)C1(C)C	0.400	1.600	1.476E-05	1.1832	1.868E-12
C811OH	OCC1CC(C(=O)O)C1(C)C	0.376	1.750	7.291E-04	1.1425	3.301E-11
C813OOH	OCC(CC(=O)C(=O)O)C(C)(C)OO	0.750	1.750	4.307E-08	1.2764	2.294E-10
ALDOL dimer	CC(=O)C(=O)CC(C(C=O)=CCC1CC(C(O)=O)C1(C)C)C(C)(C)OO	0.368	1.474	1.387E-12	1.1974	4.602E-11
ESTER dimer	CC1(C)C(CC1C(O)=O)CC(=O)OCC(=O)C2CC(CC(O)=O)C2(C)C	0.368	1.474	2.073E-12	1.1974	1.152E-10
Malic acid	OC(CC(O)=O)C(O)=O	1.250	1.500	4.012E-06	1.4526	4.827E-10
Phthalic acid	O=C(O)C1=CC=CC=C1C(O)=O	0.500	0.750	4.165E-06	1.4398	5.565E-10
Ammonium Sulphate	O=S([O-])([O-])=O.[NH4+].[NH4+]	-	-	non-volatile	1.55 (l.) [f] 1.77 (s.)	2.250E-09 or 0.0 [g]
Sulphuric acid	OS(=O)(=O)O	-	-	non-volatile	1.856 (l.) [h]	3.031E-09 or 0.0 [g]

[a] Name of the molecule as defined by the Master Chemical Mechanism (MCM), version 3.1. Most of the SOA surrogate compounds (those derived from the ozonolysis of α-pinene) are taken from Zuend and Seinfeld[64].

[b] Pure component liquid-state vapour pressure predicted by the EVAPORATION model[93] (available online at: http://tropo.aeronomie.be/models/evaporation_run.htm).

[c] Liquid-state pure component density at 288 K, according to the predictive method of Girolami[97]; calculated by using the UManSysProp property predictive techniques online tool (http://umansysprop.seaes.manchester.ac.uk; by Topping et al.[98].

[d] Total molar concentration amounts, n^{t}, (sum of gas + particle amounts) in mol per m^{3} of air. These amounts constrain the input to the gas-particle partitioning model together with the RH-dependent molar amount for water, the model then determines the compositions of gas and liquid phases at equilibrium.

[e] Vapour pressure of liquid water based on parameterisation by Murphy and Koop[99].

[f] The apparent ammonium sulphate density in the liquid state (l.) as extrapolated from liquid aqueous solutions and the solid (crystalline) state (s.) density, both based on data from Clegg and Wexler[100].

[g] Either ammonium sulphate or sulphuric acid is used to represent the inorganic sulphate component in the particles (but not both).

[h] Liquid state density of pure sulphuric acid at T = 288.15 K, determined using the parameterisation by Myhre et al.[101] [101] [101] [101] [101] [100] [69] [69]

Table S3.2. Molecular properties and system composition of the simplified set of SOA surrogate components, enriched in high-molecular-mass dimer compounds, water and ammonium sulphate or sulfuric acid, used for the thermodynamic equilibrium model calculations. See also footnotes to Table S1.

Name	Molecular structure (SMILES)	O:C	H:C	p° [Pa] at T=288.15 K	Density [g cm^{-3}]	n^{t} [mol m^{-3}]
Water	[H]O[H]	-	-	1.706E+03	0.9971	RH-dependent
ALDOL dimer	CC(=O)C(=O)CC(C(C=O)=CCC1CC(C(O)=O)C1(C)C)C(C)(C)OO	0.368	1.474	1.387E-12	1.1974	3.54E-10
ESTER dimer	CC1(C)C(CC1C(O)=O)CC(=O)OCC(=O)C2CC(CC(O)=O)C2(C)C	0.368	1.474	2.073E-12	1.1974	3.54E-10
Malic acid	OC(CC(O)=O)C(O)=O	1.250	1.500	4.012E-06	1.4526	2.32E-10
Phthalic acid	O=C(O)C1=CC=CC=C1C(O)=O	0.500	0.750	4.165E-06	1.4398	4.24E-11
Ammonium Sulphate	O=S([O-])([O-])=O.[NH4+].[NH4+]	-	-	non-volatile	1.55 (l.) 1.77 (s.)	2.25E-09 or 0.0
Sulphuric acid	OS(=O)(=O)O	-	-	non-volatile	1.856 (l.)	3.03E-09 or 0.0

Table S3.3. Summary of model configurations and resulting predictions carried out for the two surrogate systems. Both the AIOMFAC-based equilibrium predictions with consideration of LLPS as well as the predictions from the simplified organic film model are provided, all for T = 288.15 K. The organic to inorganic dry mass ratio (OIR) was ~1:1 for the listed cases (i.e., OM/SO$_4^{2-}$ dry mass ratios of ~1.03 for H$_2$SO$_4$ and ~1.38 for ammonium sulphate). The critical supersaturation ($SS*$) and diameter ($D*$) properties at cloud droplet activation are also compared to corresponding predictions for a constant surface tension value of σ = 72 mN m^{-1}.

Model, input & assumptions					Predictions			σ = 72 mN/m		Rel. dev. [c]		Remarks
System	Inorg. [a]	D_0 [nm]	$\delta_{\beta,min}$ [nm]	Model	$SS*$ [%]	$D*$ [nm]	$\sigma*$ [b] [mN/m]	SS_{72}^* [%]	D_{72}^* [nm]	$\Delta SS*$ [%]	$\Delta D*$ [%]	
1	AS	41	0.16	LLPS	0.68	223.2	66.3	0.81	175.2	-16	27	
1	AS	41	0.16	org. film	0.40	352.7	52.6	0.91	154.8	-56	128	
1	AS	41	0.30	LLPS	0.72	202.9	67.8	0.81	175.2	-10	16	Fig. S3.7.3
1	AS	41	0.30	org. film	0.51	278.6	55.8	0.91	154.8	-44	80	Fig. S3.7.3
1	H$_2$SO$_4$	41	0.16	LLPS	0.71	213.5	66.6	0.83	173.4	-14	23	
1	H$_2$SO$_4$	41	0.16	org. film	0.39	363.1	53.3	0.83	173.4	-53	109	
2	AS	41	0.16	LLPS	0.51	304.2	58.3	0.95	147.7	-47	106	Fig. S3.7.2
2	AS	41	0.16	org. film	0.45	322.1	53.8	0.96	144.9	-53	122	Fig. S3.7.2
2	H$_2$SO$_4$	41	0.16	LLPS	0.50	311.2	58.8	0.88	163.5	-44	90	Fig. 3, Fig. S3.7.1
2	H$_2$SO$_4$	41	0.16	org. film	0.43	330.2	54.3	0.88	163.7	-51	102	
2	AS	41	0.30	LLPS	0.60	245.3	59.2	0.95	147.7	-37	66	
2	AS	41	0.30	org. film	0.56	257.3	56.8	0.96	144.9	-42	78	
2	H$_2$SO$_4$	41	0.30	LLPS	0.58	252.9	59.9	0.88	163.5	-34	55	
2	H$_2$SO$_4$	41	0.30	org. film	0.54	264.7	57.3	0.88	163.7	-39	62	
2	AS	175	0.30	LLPS	0.08	2119	72.0	0.10	1400	-15	51	Fig. S3.7.4
2	AS	175	0.30	org. film	0.06	2290	57.1	0.10	1401	-38	63	Fig. S3.7.4

[a] Inorganic sulphate component at input, ammonium sulphate (AS) or sulphuric acid (H$_2$SO$_4$).

[b] The predicted surface tension at the point of droplet activation.

[c] The relative deviation of the predicted critical properties when composition-dependent surface tension is considered relative to the assumption of a constant σ = 72 mN m^{-1}. For example, $\Delta D* = \frac{D*-D_{72}^*}{D_{72}^*} \times 100\,\%$, where D_{72}^* denotes the critical diameter that was predicted for σ = 72 mN m^{-1}.

Table S3.4. Summary of model configurations and resulting predictions with regard to variation in organic to sulphate dry mass ratios (OM/SO$_4^{2-}$) for surrogate system 2, for T = 288.15 K and a total dry mass concentration of 0.6 µg/(m^3 of air). See also Table S3.3 for the meaning of the metrics listed.

Model, input & assumptions					Predictions			σ = 72 mN/m		Rel. dev.	
OM/SO$_4^{2-}$ [kg/kg]	Inorg.	D_0 [nm]	$\delta_{\beta,min}$ [nm]	Model	SS* [%]	D^* [nm]	σ^* [mN/m]	SS_{72}^* [%]	D_{72}^* [nm]	ΔSS^* [%]	ΔD^* [%]
0.786	AS	41	0.16	LLPS	0.53	287.6	60.7	0.83	168.1	-36	71
0.786	AS	41	0.16	org. film	0.47	305.7	56.1	0.83	167.5	-44	82
0.786	H$_2$SO$_4$	41	0.16	LLPS	0.51	303.6	60.2	0.82	173.2	-38	75
0.786	H$_2$SO$_4$	41	0.16	org. film	0.44	326.3	55.2	0.82	175.2	-47	86
1.941	AS	41	0.16	LLPS	0.50	311.8	57.3	1.05	133.6	-52	133
1.941	AS	41	0.16	org. film	0.43	333.2	52.1	1.07	131.3	-60	154
1.941	H$_2$SO$_4$	41	0.16	LLPS	0.49	316.9	56.4	1.07	135.2	-54	134
1.941	H$_2$SO$_4$	41	0.16	org. film	0.41	350.7	52.0	1.08	133.7	-62	162
0.786	AS	41	0.3	LLPS	0.61	242.2	62.4	0.83	168.1	-26	44
0.786	AS	41	0.3	org. film	0.57	252.2	59.5	0.83	167.5	-32	51
0.786	H$_2$SO$_4$	41	0.3	LLPS	0.59	250.7	61.4	0.82	173.2	-29	45
0.786	H$_2$SO$_4$	41	0.3	org. film	0.53	267.6	58.7	0.82	175.2	-35	53
1.941	AS	41	0.3	LLPS	0.60	246.7	57.7	1.05	133.6	-42	85
1.941	AS	41	0.3	org. film	0.55	261.5	54.8	1.07	131.3	-49	99
1.941	H$_2$SO$_4$	41	0.3	LLPS	0.59	251.0	57.0	1.07	135.2	-44	86
1.941	H$_2$SO$_4$	41	0.3	org. film	0.53	270.0	54.0	1.08	133.7	-51	102
5.666	H$_2$SO$_4$	41	0.16	LLPS	0.50	137.4	34.7	1.50	99.1	-67	39
5.666	H$_2$SO$_4$	41	0.16	org. film	0.44	134.7	30.0	1.63	93.4	-73	44
0.176	H$_2$SO$_4$	41	0.16	LLPS	0.55	273.0	67.4	0.64	221.9	-13	23
0.176	H$_2$SO$_4$	41	0.16	org. film	0.50	283.2	63.4	0.63	225.2	-21	26

Table S3.5. Total molar input compositions, n^t (mol/m^3), for aerosol total dry particle mass concentration of 0.6 μg/(m^3 of air) for the organic and sulphate components of system 2 used in the model calculations listed in Table S3.4.

Component	OM/SO$_4^{2-}$ dry mass ratio			
	15/85 (= 0.176)	44/56 (= 0.786)	66/34 (= 1.941)	85/15 (= 5.666)
ALDOL dimer	1.066E-10	3.126E-10	4.690E-10	6.040E-10
ESTER dimer	1.066E-10	3.126E-10	4.690E-10	6.040E-10
Malic acid	7.006E-11	2.379E-10	3.359E-10	4.054E-10
Phthalic acid	7.833E-11	1.124E-10	1.313E-10	1.437E-10
Sulphuric acid or ammonium sulphate	5.309E-09	3.498E-09	2.124E-09	9.369E-10

Table S3.6. Pure component liquid-state vapour pressures ($p°$) at 288.15 K estimated with three different predictive methods (EVAP, N-N, MY-N; see footnotes) for the components of surrogate system 2. The corresponding total molar input compositions (n^t) (based on the three sets of vapour pressures) are listed for an OM/SO$_4^{2-}$ dry mass ratio of 55/45 (= 1.222) and were determined for a fixed particle composition at 10 % RH and 0.6 μg/(m^3 of air) total dry particle mass concentration.

Component	$p°$ [Pa] at T = 288.15 K			n^t [mol m^{-3}]		
	EVAP [a]	N-N [b]	MY-N [c]	EVAP	N-N	MY-N
ALDOL dimer	1.387E-12	4.123E-13	9.718E-08	3.908E-10	3.908E-10	3.942E-10
ESTER dimer	2.073E-12	3.634E-12	7.388E-07	3.908E-10	3.908E-10	4.170E-10
Malic acid	4.012E-06	1.079E-05	1.337E-03	2.563E-10	2.563E-10	2.693E-10
Phthalic acid	4.165E-06	1.161E-05	4.377E-04	5.881E-11	7.421E-11	1.313E-09
Sulphuric acid	-	-	-	2.811E-09	2.811E-09	2.811E-09

[a] EVAP method: estimation of $p°$ by the EVAPORATION model of Compernolle et al.[93] (available online at: http://tropo.aeronomie.be/models/evaporation_run.htm).

[b] N-N method: estimation of $p°$ by the method of Nannoolal et al.[94] with required normal boiling point temperatures (T_b) estimated by the model of Nannoolal et al.[95]; obtained using the UManSysProp property predictive techniques online tool (http://umansysprop.seaes.manchester.ac.uk; by Topping et al.[98].

[c] MY-N method: estimation of $p°$ by the method of Myrdal and Yalkowsky[96] with T_b estimation by the model of Nannoolal et al.[95]; obtained using the UManSysProp tool.

Table S3.7. Predictions of critical CCN activation properties by the equilibrium gas-particle partitioning model with consideration of LLPS. The pure component vapour pressures and total molar input compositions were determined using three distinct methods, listed in Table S3.6. These predictions are for a dry size D_0 = 41 nm, an OM/SO$_4^{2-}$ dry mass ratio of 55/45 (= 1.222), sulphuric acid as the sulphate component and T = 288.15 K. See also Tables S3.3 and S3.6 for the meaning of the metrics listed.

Method for $p°$	$\delta_{\beta,min}$ [nm]	SS^* [%]	D^* [nm]	σ^* [mN/m]	SS_{72}^* [%]	D_{72}^* [nm]	ΔSS^* [%]	ΔD^* [%]
EVAP	0.16	0.49	315.3	58.3	0.92	155.8	-47	102
EVAP	0.3	0.59	253.1	59.1	0.92	155.8	-37	62
N-N	0.16	0.49	315.1	58.4	0.93	155.7	-47	102
N-N	0.3	0.59	252.9	59.1	0.93	155.7	-37	62
MY-N	0.16	0.53	290.3	58.5	1.00	140.8	-47	106
MY-N	0.3	0.63	232.2	59.2	1.00	140.8	-37	65

4   Comparison of Model Predictions with Bulk Measurements of Cloud Surface Tension Lowering.

4.1   Surface-tension-lowering and Organic Carbon Concentration: Comparison to other Environments.

The expected range of surface tension lowering during droplet activation as a function of carbon concentration (Total Organic Carbon – TOC), stated as parts per million (by mass) elemental carbon in the aqueous sample/particle (ppm C), is quantified from surface tension measurements of atmospheric fog and cloud-water samples collected from diverse environments ranging from the Po Valley fog in Italy, to maritime clouds in the Atlantic (Tenerife), and clouds influenced by biomass burning, and regional haze in Korea (Fig. 4.1.1).

The macroscopic cloud/fog water samples were analyzed for surface tension at 25°C temperature using a SINTECH (Berlin, Germany) PAT1 tensiometer. The measurement was based on the axial symmetric drop shape analysis[102]. Briefly, a drop of the sample was generated at the capillary tip of the tensiometer. The sample was then left to stand for 30 minutes keeping the drop surface area constant. At given time intervals, drop profiles were acquired and stored; subsequently, the surface tension value was automatically calculated according to the Laplace equation. Furthermore, aliquots of cloud and rainwater samples or aerosol extracts were evaporated under vacuum in a step-wise procedure, decreasing the volume of the liquid sample to about 1/20 – 1/100 of the original one. After each evaporation step, the surface tension was measured in order to obtain the dependence on the total soluble carbon concentration.
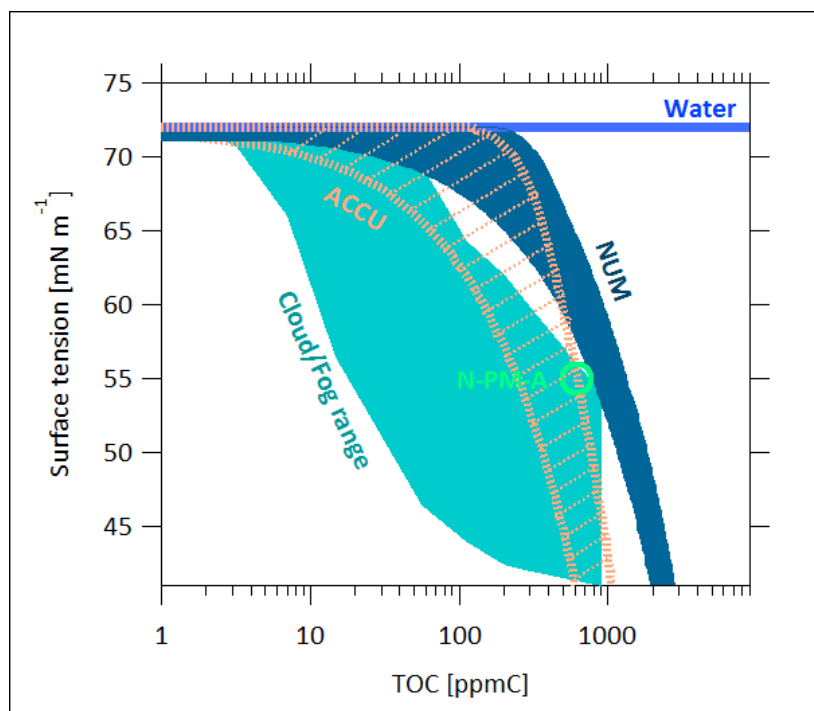
Figure S4.1.1. Fog and cloud solution surface tension (σ) as a function of total organic carbon (TOC) in the solution (light blue shaded area). Fog samples were from the Po Valley in Italy and cloud samples were from North East Atlantic (Tenerife) and Asia. Also shown is the line corresponding to the pure water surface tension and points/ranges for different model predictions: data point named 'N-PM-A' (Non-Partition Model with AMS chemical composition) - obtained by plotting surface tension that best represents our data vs. TOC calculated from AMS OM measurements in the ultrafine particle mode and scaled to the wet activation droplet diameter found from κ-Köhler theory for ammonium sulphate, enhanced by 50%[11]. The dark blue shaded area represents the range of σ-TOC variability for ultrafine mode particles (NUM) as predicted by the AIOMFAC-based thermodynamic model, where the upper limit is defined by the LLPS prediction for system 2 (see section 3.6 in SI for system description) and the lower limit is from the prediction by the simplified organic film model (see section 3.5 in SI for more details). Similarly, the light red-dashed area represents the range of σ-TOC variability, but for the accumulation mode particles (ACCU) with the upper limit from the LLPS model for system 2 and the lower limit from the simplified organic film model.

The point drawn for the organic carbon (OC) values calculated from the actual NUM composition measurements (N-PM-A) is encapsulated inside the cloud region. A total OM concentration in ultrafine particles was calculated assuming a dry particle diameter of 41nm and chemical composition derived from AMS (50% percent of particle mass was organics). An AMS derived OM/OC ratio of 1.9 was used for these calculations, which is in agreement with the OM/OC of the LLPS model systems. Resulting OC concentration in mg per particle was divided by droplet volume in liters to get mg L^{-1} ≈ ppmC. κ of ammonium sulphate (0.6)[49] was used for the N-PM-A and the wet critical CCN activation diameter, D^*, was

calculated from κ-Köhler theory. The determined D^* was then increased by 50 % in diameter according to the recent findings for surface-tension-lowering organics[58].

4.2   Comparison with LLPS and Film Model outputs

Observed values of surface tension were also reproduced by the LLPS model where the majority of surface active molecules can migrate to the surface of the droplet (particle phase β), thus reducing its surface tension. The σ-TOC (and corresponding water content) ranges derived from the thermodynamic model for the particles growing to CCN activation size and beyond for ultrafine and accumulation mode particles, NUM and ACCU, respectively, are presented in the Fig. S4.1.1 as well. The dark blue shaded area represents the range of σ-TOC variability for the NUM particles. The size of 41 nm was selected for model calculations as equivalent to the NUM. The light red dashed area corresponds to ACCU-size particles, where specifically 175 nm dry diameter was selected for the model calculations. The upper limit (right side) for both particle sizes is defined by the AIOMFAC-based LLPS model simulations for surrogate system 2 while the lower limit (left side) is derived from the AIOMFAC-based simplified organic film model for the same system (see section 3.5 in SI for more details). Low surface tension (high TOC) values relate to a full coverage by phase β. Reduced coverage (lower TOC values) results in an increase in surface tension (smaller reduction from the pure water σ_w), which ultimately reaches the σ_w of water. It is apparent that the organic film model represents a higher reduction in σ at the same TOC value when compared to the LLPS model. As discussed in Section 3, it can be concluded that the combination of these two model predictions describe the limits for expected σ vs. TOC effects for a given particle dry size and chemical composition.

The predicted LLPS surrogate system 2 NUM TOC ranges are located outside the cloud/fog range, which can be explained by differences in the systems. In a bulk cloud water sample, most of the organic mass will be contributed by the organic mass initially present in accumulation mode particles (forming cloud droplets upon activation) and the organic mass contribution from activated ultrafine mode particles is negligible in comparison. Thus, it is reasonable to assume that the TOC in a macroscopic sample, obtained from the coalescence of a huge number of cloud droplets during the sampling period, will be defined primarily by

the accumulation of organic mass stemming from accumulation mode particles, while the LLPS model describes here the conditions of single microscopic particles (no coalescence), as discussed above. In order to at least partially mimic the macroscopic approach for comparison, the calculated surface tension vs. TOC of accumulation mode particles were taken into account with the LLPS model. An σ-TOC range representing accumulation mode particles (e.g. D_0=175 nm), as found in ambient size distribution measurements, is presented as ACCU in Fig. S4.1.1. These TOC and σ ranges agree quite well with the higher TOC boundary of the macroscopic cloud/fog range shown in Fig. S4.1.1. The lower TOC boundary of the cloud/fog range at a certain σ is more representative of the combined effects of the coalescence of millions of cloud droplets to form a macroscopic cloud water sample (approximately preserving the TOC of an average cloud droplet) alongside a substantial decrease in surface/volume ratio in such a sample compared to a microscopic particle/cloud droplet. The relatively small surface/volume ratio of the macroscopic sample allows a relatively small concentration of surfactants to cover the sample surface (creating an organic film / phase) and to cause a substantial lowering in surface tension already at low TOC levels.

After activation, an accumulation mode particle will grow further into a cloud droplet with a lower TOC (due to increasing dilution by water) and higher surface tension (following the dashed light red area in the Fig. S4.1.1 toward the σ_w value for pure water), which would be in reasonable agreement with the Szyszkowski-Langmuir relationship and curve shown in Facchini et al.[103] as well as the higher TOC cloud/fog range boundary shown in Fig. S4.1.1. This accumulation mode example shows that AIOMFAC-based model predictions with LLPS consideration tend to agree with the macroscopic cloud/fog water data range when the applied conditions are more comparable. This then also provides an explanation for the much higher TOC for model surrogate system 2 for the ultrafine particle case with dry diameter of 41 nm and variable σ (ranging from ~35 to 72 mN m^{-1} during the growth process), because for the ultrafine particles, the water content at activation size and prior to that is relatively small, leading to high TOC.

References

33 O'Dowd, C., Monahan, C. & Dall'Osto, M. On the occurrence of open ocean particle production and growth events. *Geophys Res Lett* **37**, L19805, *10.1029/2010GL044679* (2010).

34 Draxler, R. R. a. R., G.D. HYSPLIT (HYbrid Single-Particle Lagrangian Integrated Trajectory) Model access via NOAA ARL READY Website (2013).

35 DeCarlo, P. F. *et al.* Field-deployable, high-resolution, time-of-flight aerosol mass spectrometer. *Anal Chem* **78**, 8281-8289, *10.1021/Ac061249n* (2006).

36 Bahreini, R. *et al.* Organic aerosol formation in urban and industrial plumes near Houston and Dallas, Texas. *J Geophys Res-Atmos* **114**, *Artn D00f16*

Doi 10.1029/2008jd011493 (2009).

37 Jimenez, J. L. *et al.* Comment on "The effects of molecular weight and thermal decomposition on the sensitivity of a thermal desorption aerosol mass spectrometer". *Aerosol Sci Tech* **50**, i-xv, *10.1080/02786826.2016.1205728* (2016).

38 Monahan, C., Vuollekoski, H., Kulmala, M. & O'Dowd, C. Simulating Marine New Particle Formation and Growth Using the M7 Modal Aerosol Dynamics Modal. *Advances in Meteorology*, *10.1155/2010/689763* (2010).

39 Bialek, J., Dall'Osto, M., Monahan, C., Beddows, D. & O'Dowd, C. On the contribution of organics to the North East Atlantic aerosol number concentration. *Environ Res Lett* **7**, *10.1088/1748-9326/7/4/044013* (2012).

40 Jimenez, J. L. *et al.* Ambient aerosol sampling using the Aerodyne Aerosol Mass Spectrometer. *J Geophys Res-Atmos* **108**, 8425, *DOI:10.1029/2001JD001213* (2003).

41 Kulmala, M. How Particles Nucleate and Grow. *Science* **302**, 1000-1001, *10.1126/science.1090848* (2003).

42 Middlebrook, A. M., Bahreini, R., Jimenez, J. L. & Canagaratna, M. R. Evaluation of composition-dependent collection efficiencies for the aerodyne aerosol mass spectrometer using field data. *Aerosol Sci Tech* **46**, 258–271, *doi:10.1080/02786826.2011.620041* (2012).

43 DeCarlo, P. F., Slowik, J. G., Worsnop, D. R., Davidovits, P. & Jimenez, J. L. Particle morphology and density characterization by combined mobility and aerodynamic diameter measurements. Part 1: Theory. *Aerosol Sci Tech* **38**, 1185-1205, *Doi 10.1080/027868290903907* (2004).

44 Wang, S. C. & Flagan, R. C. Scanning electrical mobility spectrometer. *J Aerosol Sci* **20**, 1485-1488, *http://dx.doi.org/10.1016/0021-8502(89)90868-9* (1989).

45 Wiedensohler, A. *et al.* Mobility particle size spectrometers: harmonization of technical standards and data structure to facilitate high quality long-term observations of atmospheric particle number size distributions. *Atmos Meas Tech* **5**, 657-685, *10.5194/amt-5-657-2012* (2012).

46 de Leeuw, G. *et al.* Production flux of sea spray aerosol. *Rev Geophys* **49**, RG2001, *doi:10.1029/2010rg000349* (2011).

47 Ovadnevaite, J. *et al.* A sea spray aerosol flux parameterization encapsulating wave state. *Atmos Chem Phys* **14**, 1837-1852, *10.5194/acp-14-1837-2014* (2014).

48 O'Dowd, C. D. *et al.* Biogenically driven organic contribution to marine aerosol. *Nature* **431**, 676-680, *DOI:10.1038/Nature02959* (2004).

49 Petters, M. D. & Kreidenweis, S. M. A single parameter representation of hygroscopic growth and cloud condensation nucleus activity. *Atmos. Chem. Phys.* **7**, 1961-1971, *10.5194/acp-7-1961-2007* (2007).

50 Zuend, A., Marcolli, C., Luo, B. P. & Peter, T. A thermodynamic model of mixed organic-inorganic aerosols to predict activity coefficients. *Atmos. Chem. Phys.* **8**, 4559-4593, *10.5194/acp-8-4559-2008* (2008).

51 Zuend, A. *et al.* New and extended parameterization of the thermodynamic model AIOMFAC: calculation of activity coefficients for organic-inorganic mixtures containing carboxyl, hydroxyl, carbonyl, ether, ester, alkenyl, alkyl, and aromatic functional groups. *Atmos. Chem. Phys.* **11**, 9155-9206, *10.5194/acp-11-9155-2011* (2011).

52 Nakao, S., Suda, S. R., Camp, M., Petters, M. D. & Kreidenweis, S. M. Droplet activation of wet particles: development of the Wet CCN approach. *Atmos. Meas. Tech.* **7**, 2227-2241, *10.5194/amt-7-2227-2014* (2014).

53 Hodas, N. *et al.* Discontinuities in hygroscopic growth below and above water saturation for laboratory surrogates of oligomers in organic atmospheric aerosols. *Atmos. Chem. Phys.* **16**, 12767-12792, *10.5194/acp-16-12767-2016* (2016).

54 Zana, R. Dimeric and oligomeric surfactants. Behavior at interfaces and in aqueous solution: a review. *Advances in Colloid and Interface Science* **97**, 205-253, http://dx.doi.org/10.1016/S0001-8686(01)00069-0 (2002).

55 Schwier, A. N., Viglione, G. A., Li, Z. & Faye McNeill, V. Modeling the surface tension of complex, reactive organic–inorganic mixtures. *Atmos. Chem. Phys.* **13**, 10721-10732, *10.5194/acp-13-10721-2013* (2013).

56 Romakkaniemi, S. *et al.* Partitioning of semivolatile surface-active compounds between bulk, surface and gas phase. *Geophys Res Lett* **38**, *10.1029/2010GL046147* (2011).

57 Xu, W. *et al.* Cloud forming potential of oligomers relevant to secondary organic aerosols. *Geophys Res Lett* **41**, 6538-6545, *10.1002/2014GL061040* (2014).

58 Ruehl, C. R., Davies, J. F. & Wilson, K. R. An interfacial mechanism for cloud droplet formation on organic aerosols. *Science* **351**, 1447-1450, *10.1126/science.aad4889* (2016).

59 Kohler, H. The nucleus in and the growth of hygroscopic droplets. *Transactions of the Faraday Society* **32**, 1152-1161, *10.1039/TF9363201152* (1936).

60 Lei, T., Zuend, A., Wang, W. G., Zhang, Y. H. & Ge, M. F. Hygroscopicity of organic compounds from biomass burning and their influence on the water uptake of mixed organic ammonium sulfate aerosols. *Atmos. Chem. Phys.* **14**, 11165-11183, *10.5194/acp-14-11165-2014* (2014).

61 Zuend, A., Marcolli, C., Peter, T. & Seinfeld, J. H. Computation of liquid-liquid equilibria and phase stabilities: implications for RH-dependent gas/particle partitioning of organic-inorganic aerosols. *Atmos. Chem. Phys.* **10**, 7795-7820, *DOI 10.5194/acp-10-7795-2010* (2010).

62 Topping, D. & McFiggans, G. Tight coupling of particle size, number and composition in atmospheric cloud droplet activation. *Atmospheric Chemistry and Physics* **12**, 3253-3260, (2012).

63 Topping, D., Connolly, P. & McFiggans, G. Cloud droplet number enhanced by co-condensation of organic vapours. *Nature Geosci.* **6**, 443-446, *10.1038/ngeo1809* (2013).

64 Zuend, A. & Seinfeld, J. H. Modeling the gas-particle partitioning of secondary organic aerosol: the importance of liquid-liquid phase separation. *Atmos. Chem. Phys.* **12**, 3857-3882, *10.5194/acp-12-3857-2012* (2012).

65 Zuend, A. & Seinfeld, J. H. A practical method for the calculation of liquid–liquid equilibria in multicomponent organic–water–electrolyte systems using physicochemical constraints. *Fluid Phase Equilibria* **337**, 201-213, *10.1016/j.fluid.2012.09.034* (2013).

66 Song, M., Marcolli, C., Krieger, U. K., Lienhard, D. M. & Peter, T. Morphologies of mixed organic/inorganic/aqueous aerosol droplets. *Faraday Discussions* **165**, 289-316, *10.1039/C3FD00049D* (2013).

67   Altaf, M. B., Zuend, A. & Freedman, M. A. Role of nucleation mechanism on the size dependent morphology of organic aerosol. *Chemical Communications*, *10.1039/C6CC03826C* (2016).

68   Harkins, W. D. A general thermodynamic theory of the spreading of liquids to form duplex films and of liquids or solids to form monolayers. *The Journal of Chemical Physics* **9**, 552-568, (1941).

69   Reid, J. P. *et al.* The morphology of aerosol particles consisting of hydrophobic and hydrophilic phases: hydrocarbons, alcohols and fatty acids as the hydrophobic component. *Phys. Chem. Chem. Phys.* **13**, 15559-15572, *10.1039/C1CP21510H* (2011).

70   Kwamena, Buajarern, J. & Reid, J. P. Equilibrium Morphology of Mixed Organic/Inorganic/Aqueous Aerosol Droplets: Investigating the Effect of Relative Humidity and Surfactants. *J. Phys. Chem. A* **114**, 5787-5795, (2010).

71   McFiggans, G. *et al.* The effect of physical and chemical aerosol properties on warm cloud droplet activation. *Atmos. Chem. Phys.* **6**, 2593-2649, *10.5194/acp-6-2593-2006* (2006).

72   Vargaftik, N. B., Volkov, B. N. & Voljak, L. D. International Tables of the Surface Tension of Water. *Journal of Physical and Chemical Reference Data* **12**, 817-820, *10.1063/1.555688* (1983).

73   Poling, B. E., Prausnitz, J. M., O'Connell, J. P. & Reid, R. C. *The properties of gases and liquids*. 5 edn, (McGraw-Hill, 2001).

74   Álvarez, E., Vázquez, G., Sánchez-Vilas, M., Sanjurjo, B. & Navaza, J. M. Surface tension of organic acids+ water binary mixtures from 20 C to 50 C. *Journal of Chemical & Engineering Data* **42**, 957-960, (1997).

75   Riipinen, I. *et al.* Adipic and Malonic Acid Aqueous Solutions: Surface Tensions and Saturation Vapor Pressures. *The Journal of Physical Chemistry A* **111**, 12995-13002, *10.1021/jp073731v* (2007).

76   Chumpitaz, L. D. A., Coutinho, L. F. & Meirelles, A. J. A. Surface tension of fatty acids and triglycerides. *Journal of the American Oil Chemists' Society* **76**, 379-382, *10.1007/s11746-999-0245-6* (1999).

77   Ruehl, C. R. *et al.* Strong evidence of surface tension reduction in microscopic aqueous droplets. *Geophysical Research Letters* **39**, n/a-n/a, *10.1029/2012GL053706* (2012).

78   Topping, D. O. *et al.* Surface tensions of multi-component mixed inorganic/organic aqueous systems of atmospheric significance: measurements, model predictions and importance for cloud activation predictions. *Atmos. Chem. Phys.* **7**, 2371-2398, *10.5194/acp-7-2371-2007* (2007).

79   Bondi, A. Van der Waals volumes and radii. *The Journal of Physical Chemistry* **68**, 441-451, (1964).

80   Ruehl, C. R. & Wilson, K. R. Surface organic monolayers control the hygroscopic growth of submicrometer particles at high relative humidity. *The Journal of Physical Chemistry A* **118**, 3952-3966, (2014).

81   Aiken, A. C. *et al.* O/C and OM/OC ratios of primary, secondary, and ambient organic aerosols with high-resolution time-of-flight aerosol mass spectrometry. *Environ. Sci. Technol.* **42**, (2008).

82   Fu, P. Q., Kawamura, K., Chen, J., Charriere, B. & Sempere, R. Organic molecular composition of marine aerosols over the Arctic Ocean in summer: contributions of primary emission and secondary aerosol formation. *Biogeosciences* **10**, 653-667, *DOI 10.5194/bg-10-653-2013* (2013).

83   Decesari, S., Facchini, M. C., Fuzzi, S. & Tagliavini, E. Characterization of water-soluble organic compounds in atmospheric aerosol: A new approach. *Journal of Geophysical Research: Atmospheres* **105**, 1481-1489, *10.1029/1999JD900950* (2000).

84 Zhang, X. *et al.* Formation and evolution of molecular products in α-pinene secondary organic aerosol. *Proceedings of the National Academy of Sciences* **112**, 14168-14173, *10.1073/pnas.1517742112* (2015).

85 Ehn, M. *et al.* A large source of low-volatility secondary organic aerosol. *Nature* **506**, 476-479, *10.1038/nature13032* (2014).

86 Schobesberger, S. *et al.* Molecular understanding of atmospheric particle formation from sulfuric acid and large oxidized organic molecules. *Proceedings of the National Academy of Sciences* **110**, 17223-17228, *10.1073/pnas.1306973110* (2013).

87 Renbaum-Wolff, L. *et al.* Observations and implications of liquid–liquid phase separation at high relative humidities in secondary organic material produced by α-pinene ozonolysis without inorganic salts. *Atmos. Chem. Phys.* **16**, 7969-7979, *10.5194/acp-16-7969-2016* (2016).

88 Valorso, R. *et al.* Explicit modelling of SOA formation from a-pinene photooxidation: sensitivity to vapour pressure estimation. *Atmos. Chem. Phys.* **11**, (2011).

89 Bilde, M. *et al.* Saturation Vapor Pressures and Transition Enthalpies of Low-Volatility Organic Molecules of Atmospheric Relevance: From Dicarboxylic Acids to Complex Mixtures. *Chemical Reviews* **115**, 4115-4156, *10.1021/cr5005502* (2015).

90 Huisman, A. J., Krieger, U. K., Zuend, A., Marcolli, C. & Peter, T. Vapor pressures of substituted polycarboxylic acids are much lower than previously reported. *Atmos. Chem. Phys.* **13**, 6647-6662, *10.5194/acp-13-6647-2013* (2013).

91 Barley, M. H. & McFiggans, G. The critical assessment of vapour pressure estimation methods for use in modelling the formation of atmospheric organic aerosol. *Atmos. Chem. Phys.* **10**, 749-767, (2010).

92 O'Meara, S., Booth, A. M., Barley, M. H., Topping, D. & McFiggans, G. An assessment of vapour pressure estimation methods. *Physical Chemistry Chemical Physics* **16**, 19453-19469, *10.1039/C4CP00857J* (2014).

93 Compernolle, S., Ceulemans, K. & Muller, J. F. EVAPORATION: a new vapour pressure estimation methodfor organic molecules including non-additivity and intramolecular interactions. *Atmos. Chem. Phys.* **11**, 9431-9450, *10.5194/acp-11-9431-2011* (2011).

94 Nannoolal, Y., Rarey, J. & Ramjugernath, D. Estimation of pure component properties - Part 3. Estimation of the vapor pressure of non-electrolyte organic compounds via group contributions and group interactions. *Fluid Phase Equilib.* **269**, (2008).

95 Nannoolal, Y., Rarey, J., Ramjugernath, D. & Cordes, W. Estimation of pure component properties Part 1. Estimation of the normal boiling point of non-electrolyte organic compounds via group contributions and group interactions. *Fluid Phase Equilib.* **226**, 45-63, (2004).

96 Myrdal, P. B. & Yalkowsky, S. H. Estimating Pure Component Vapor Pressures of Complex Organic Molecules. *Industrial & Engineering Chemistry Research* **36**, 2494-2499, *10.1021/ie950242l* (1997).

97 Girolami, G. S. A Simple "Back of the Envelope" Method for Estimating the Densities and Molecular Volumes of Liquids and Solids. *Journal of Chemical Education* **71**, 962, *10.1021/ed071p962* (1994).

98 Topping, D. *et al.* UManSysProp v1.0: an online and open-source facility for molecular property prediction and atmospheric aerosol calculations. *Geosci. Model Dev.* **9**, 899-914, *10.5194/gmd-9-899-2016* (2016).

99 Murphy, D. M. & Koop, T. Review of the vapour pressures of ice and supercooled water for atmospheric applications. *Quarterly Journal of the Royal Meteorological Society* **131**, 1539-1565, *10.1256/qj.04.94* (2005).

100 Clegg, S. L. & Wexler, A. S. Densities and Apparent Molar Volumes of Atmospherically Important Electrolyte Solutions. 1. The Solutes H2SO4, HNO3, HCl, Na2SO4, NaNO3, NaCl, (NH4)2SO4, NH4NO3, and NH4Cl from 0 to 50 °C, Including Extrapolations to Very Low Temperature and to the Pure Liquid State, and NaHSO4, NaOH, and NH3 at 25 °C. *The Journal of Physical Chemistry A* **115**, 3393-3460, *10.1021/jp108992a* (2011).

101 Myhre, C. E., Nielsen, C. J. & Saastad, O. W. Density and surface tension of aqueous H2SO4 at low temperature. *Journal of Chemical & Engineering Data* **43**, 617-622, (1998).

102 Loglio, G. *et al.* in *Studies in Interface Science* Vol. Volume 11 (eds D. Möbius & R. Miller) 439-483 (Elsevier, 2001).

103 Facchini, M. C., Mircea, M., Fuzzi, S. & Charlson, R. J. Cloud albedo enhancement by surface-active organic solutes in growing droplets. *Nature* **401**, 257-259, (1999).